Emplacement of metamorphic core complexes and associated geothermal systems controlled by slab dynamics

Vincent Roche, Pietro Sternai, Laurent Guillou-Frottier, Armel Menant, Laurent Jolivet, Vincent Bouchot, Taras Gerya

Earth and Planetary Science Letters
Volume 498, 15 September 2018, Pages 322-333

Emplacement of metamorphic core complexes and associated geothermal systems controlled by slab dynamics

VincentRoche[abc]
PietroSternai[d]
LaurentGuillou-Frottier[cab]
ArmelMenant[e]
LaurentJolivet[f]
VincentBouchot[cab]
TarasGerya[g]

[a] Université d'Orléans, ISTO, UMR 7327, 45071, Orléans, France
[b] CNRS/INSU, ISTO, UMR 7327, 45071 Orléans, France
[c] BRGM, ISTO, UMR 7327, BP 36009, 45060 Orléans, France
[d] Department of Earth Sciences, University of Geneva, Switzerland
[e] Institut de Physique du Globe de Paris, Sorbonne Paris Cité, Univ. Paris Diderot, CNRS, 75005 Paris, France
[f] Sorbonne Universités, UPMC Univ. Paris 06, CNRS, Institut des Sciences de la Terre de Paris (iSTeP), 4 place Jussieu 75005 Paris, France
[g] Institute of Geophysics – Swiss Federal Institute of Technology (ETH), Zürich, Switzerland

https://doi.org/10.1016/j.epsl.2018.06.043

ABSTRACT

Slab rollback results in the development of low-angle normal faults (detachments) and metamorphic core complexes (MCCs) in back-arc domains. Although the mechanical consequences of slab dynamics on lithospheric and crustal behaviors have already been studied,

thermal effects have not been investigated yet. This study shows that slab rollback produces lithospheric-scale thermal perturbations intrinsically associated with emplacement of amagmatic high-enthalpy geothermal systems. Using a multi-scale numerical modeling approach, with lithospheric-scale 3-D thermo-mechanical models of subduction, and 2-D models of fluid flow at the scale of detachments, we demonstrate that subduction-induced extensional tectonics controls the genesis and distribution of crustal-scale thermal domes from the base of the crust, and the location of high-energy geothermal systems. We find that when slab tearing occurs, Moho temperatures can temporarily increase by up to 250 °C due to significant shear heating in the flowing upper mantle. Associated thermal anomalies (with characteristic width and spacing of tens and hundreds of km, for crustal and lithospheric scales, respectively) then migrate systematically toward the retreating trench. These thermal domes weaken the crust, localize deformation and enhance the development of crustal-scale detachments. These thermo-mechanical instabilities mimic genesis of high-temperature MCCs with migmatitic cores in the back-arc domain, such as those of the Menderes (western Anatolia, Turkey) and Larderello (southern Tuscany) provinces in the Mediterranean realm, and those in the Basin and Range (western United States), where detachments control the bulk of the heat transport. At the scale of MCCs, the bulk fluid flow pattern is controlled by topography-driven flow while buoyancy-driven flow dominates within the permeable detachments, focusing reservoir location of high-energy geothermal systems at shallow depth beneath the detachments.

1. INTRODUCTION

The development of geothermal power plants has been increasing since the 1970s, building upon more than 100 years of history in geothermal energy extraction. Currently, the

installed global capacity is estimated at 12.6 GWe (Gigawatt electrical), and forecasts for 2050 point to a worldwide capacity of 140 GWe, approximately 8.3% of total world electricity production (Bertani, 2016). Many of the high enthalpy geothermal resources (HEGRs) that make such an ambitious goal possible are located in the vicinity of subduction zones and volcanic arcs, where both magmatic and tectonic processes operate (Fig. 1). Others are located in "amagmatic" provinces such as the Menderes Massif in Western Turkey and the Basin and Range in the Western United States. Particularly noteworthy for this study is that while geothermal systems associated with magmatism have been studied in detail (e.g. Cumming, 2009) those located in "amagmatic" provinces have received less attention (Moeck *et al.*, 2014; Roche *et al.* submitted).

Recent to present (i.e. Pliocene-Quaternary) magmatism in the upper crust across the Menderes Massif and the Basin and Range is rare (Blackwell *et al.*, 2009; Faulds *et al.*, 2010) compared to that of the Larderello geothermal field, located in the southern Tuscany (i.e. Italy) (Santilano *et al.*, 2015) (Fig. 1). Open discussions on the possible role of hidden magmatic intrusions on these geothermal systems remains debated. Even if present, however, magmatic intrusions alone cannot explain the extent of these geothermal provinces (several thousand km^2 each), and therefore cannot account for high concentration of HEGRs. We must thus identify other sources of heat (deeper and larger-scale) possibly associated with deep, large-scale geodynamic processes involved by the nearby subduction systems.

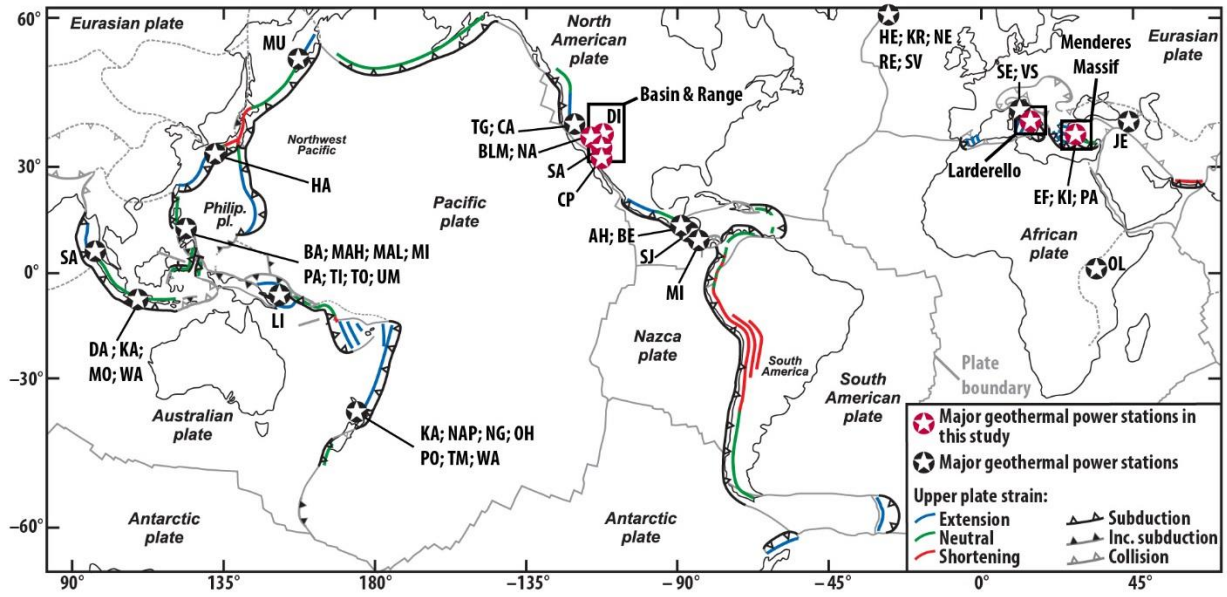

Figure 1: The major subduction zones on Earth (modified from Schellart *et al.* 2007). Black stars show the locations of major geothermal power stations that are larger than 50 MWe that are currently operational or under construction. Red stars are reserved for highlighting those within the study areas mentioned in this study. Geothermal stations: JE, Jermaghbyur (Armenia); Mi, Miravalles (Costa Rica); AH, Ahuachapán, BE, Berlín (El Salvador); HE, Hellisheidi, KR, Krafla, NE, Nesjavellir, RE, Reykjanes, SV, Svartsengi (Iceland); DA, Darajat, KA, Kamojang, MO, Mount Salak, SA, Sarulla, WA, Wayang Windu (Indonesia) ; LA, Larderello, SE, Serrazzano, VS, Valle Secolo (Italy) ; HA, Hatchobaru (Japan); OL, Olkaria (Kenya); CP, Cerro Prieto (Mexico); KA, Kawerau, NAP, Nga Awa Purua, NG, Ngatamariki, OH, Ohaaki, PO, Poihipi, TM, Te Mihi, WA, Wairakei (New Zealand); SJ, San Jacinto Tizate (Nicaragua); LI, Linhir (Papua New Guinea); BA, Bacman I, MAH, Mahanagdong, MAL, Malitbog, MI, Mindanao I-II, PA, Palinpinon I-II, TI, Tiwi A-B-C, TO, Tongonan 1, UM, Upper Mahiao (Philippines); MU, Mutnovskaya, Russia; EF, Efeler, KI, Kızıldere, PA, Pamukören (Turkey); BLM, CA, Calistoga, DV, Dixie Valley, NA, Navy, SA, Salton Sea, TG, The Geysers (United States).

Slab rollback induces lithospheric extension in the overriding plate where low-angle normal faults (detachments) control both the exhumation of metamorphic core complexes (MCCs) and the magma ascent and/or fluid circulation (e.g. Reynolds and Lister, 1987; Huet *et*

al., 2011). Because detachments may correspond to permeable structures deeply rooted down to the brittle-ductile transition (Famin *et al.*, 2004; Mezri *et al.*, 2015), active extensional domains in back-arc regions could represent favorable settings for HEGRs. The possible sources of heat responsible for regional high temperature-low pressure (HT-LP) metamorphic overprint recorded in these MCCs include (i) heating associated with thermal diffusion of excess heat generated by nappe stacking (increased radiogenic crustal heat, e.g. Bousquet *et al.*, 1997), (ii) shear-heating in the mantle (e.g. Schubert and Yuen, 1978), or (iii) advection of hot asthenosphere to shallow depths during slab retreat (Wannamaker *et al.*, 2008; Jolivet *et al.*, 2015). However, no unifying mechanism responsible for both the generation of MCCs and emplacement of high-enthalpy geothermal systems in the same regions has yet been recognized. This is however a crucial question since HEGRs represent a major economic interest in terms of exploration for carbon-free energy resources.

Here, we first document the self-consistent formation of crustal domes in the overriding plate as a result of thermo-mechanical instabilities in 3-D numerical simulations of ocean-continent subduction dynamics. These models provide crucial thermal constraints for the mantle and crust, and show the importance of shear heating and fast mantle flow on the overall heat budget. Subduction-induced thermal signature in the overriding crust obtained from these experiments is then used as basal thermal boundary condition in 2-D numerical models dedicated to the understanding of fluid flow in the upper crust in presence of detachments that accommodate the formation of these domes. Results show that deep upper crustal hot fluids are drained upward by the permeable detachment. These results will be first compared with geological observations from the Menderes Massif, and then in the discussion, with other cases in the Mediterranean realm (Anatolia and Tuscany) and in the western United States.

2. GEODYNAMIC AND GEOTHERMAL SETTINGS OF THE MENDERES MASSIF

During the Cenozoic, the eastern Mediterranean region (Figs. 2a and 2b) has undergone a two-step tectono-metamorphic evolution. In the late Cretaceous-Eocene, the convergence of Africa and Eurasia first led to the closure of the Izmir-Ankara Ocean. At this time, the accretion of subducting continental and oceanic tectonic units (e.g. Jolivet and Brun, 2010) led toformation of a south-verging crustal-scale orogenic wedge. Since the Oligo-Miocene, collapse of the Hellenides-Taurides belt in this region is mainly controlled by the southward retreat of the African slab, further accelerated in the middle Miocene by a major slab tearing event evidenced by tomographic models below western Turkey (Fig. 2c) (e.g. Piromallo and Morelli, 2003). Extension in the overriding plate has thus led to exhumation of different MCCs such as the Cyclades in the Aegean Sea and the Menderes Massif in western Anatolia, accommodated by crustal-scale low-angle normal faults such as the Simav, Alaşehir and Büyük Menderes detachments (Hetzel *et al.*, 1995; Bozkurt *et al.*, 2011) (Figs. 2b and 2c). Currently, plate kinematics in this region are characterized by more localized extension, mainly controlled by the westward motion of Anatolia (Reilinger *et al.*, 2006) and by N-S extension accommodated by steep normal faults in the Gediz and Büyük Menderes Grabens, both consequences of slab dynamics (e.g. Jolivet *et al.* 2013; Gessner *et al.*, 2013; Sternai *et al.*, 2014).

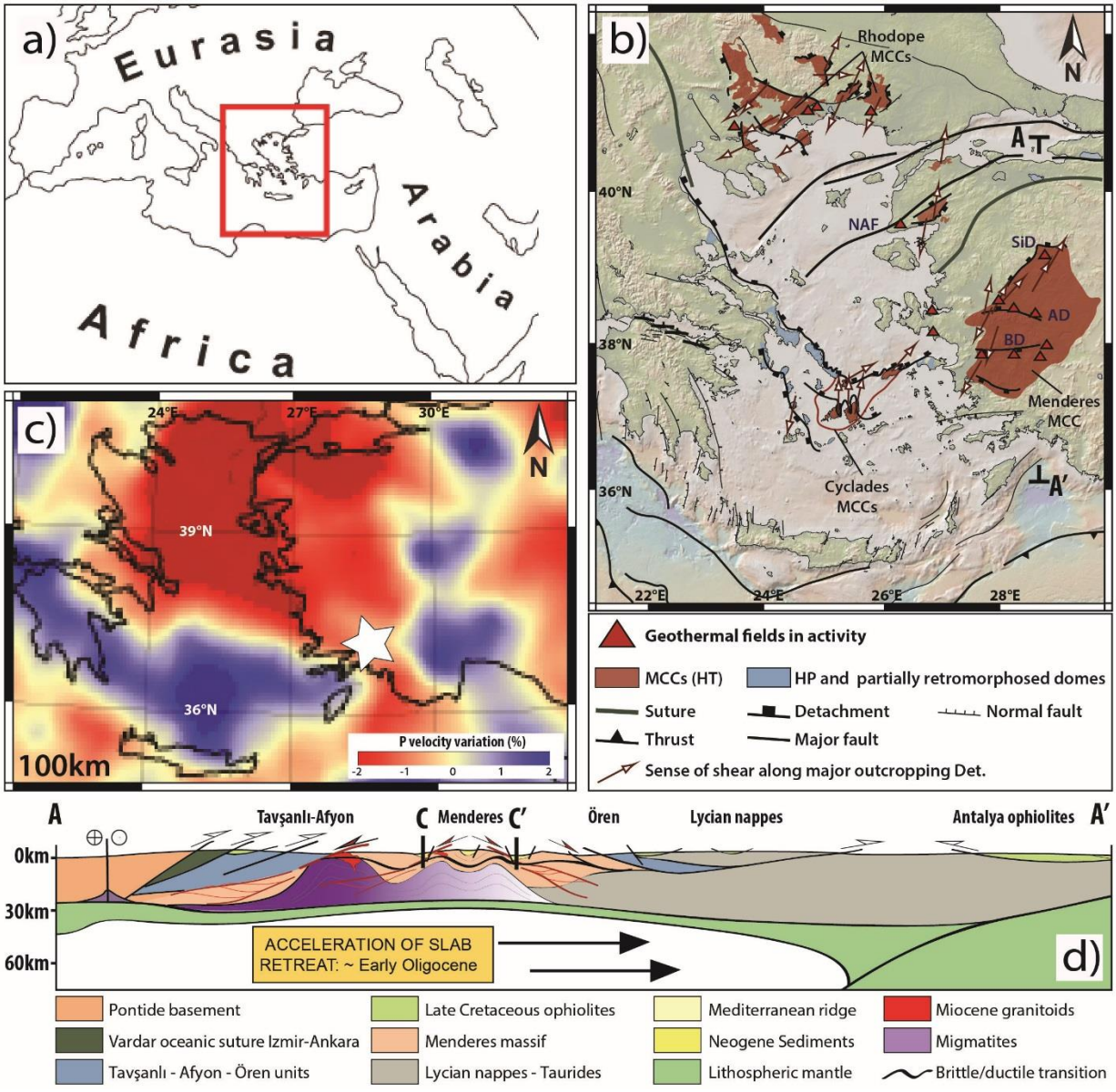

Figure 2: (a) Global map with red box showing the location on the study area. (b) Simplified tectonic maps showing the main metamorphic core complexes and associated detachments faults in the Aegean region (modified from Jolivet *et al.*, (2015)). SiD: Simav Detachment, AD: Alaşehir Detachment, BD: Büyük Detachment, NAF: North Anatolian Fault. (c) Tomographic models from Piromallo and Morelli (2003) showing the Vp anomalies at the 100 km depth. White star shows the location of a slab tear below the Menderes Massif. (d) Simplified cross-sections highlighting slab retreat and formation of crustal detachments. CC' corresponds to the 2-D numerical model cross-section.

The Menderes Massif is also recognized as an active geothermal area (see Fig. S1a in Appendix 1). This region is characterized by long wavelength east-west variations of surface heat flow density with values locally exceeding 90 mW m^{-2} (Erkan, 2015). At depth, it seems that a similar east-west long wavelength thermal anomaly is also present, as suggested by the Curie-point isotherm map of Aydin *et al.* (2005). According to these authors, the depth of the 580 °C isotherm would be lower than 10 km in western Anatolia (see Fig. S1b in Appendix 1). It turns out that most of the geothermal systems in Turkey are located in the Menderes Massif (Fig. 2b) where recent magmatism is almost absent. Here, geothermal fields are characterized by medium- to high-enthalpy, with reservoir temperature values ranging from 120 to 287 °C (e.g. Roche *et al.* in revision). Most are used for district heating systems (e.g. Balçova and Salihli), whereas a few are exploited for electricity production (e.g. Germencik, Salavatlı; Kızıldere; Alaşehir). Some authors have suggested that most of the geothermal activity can be considered as amagmatic in origin (Faulds *et al.*, 2010; Gessner *et al.*, 2017). However, Ozdemir *et al.* (2017) considered a probable magmatic intrusion in the crust to explain the heat source. Since there is presently no evidence for the existence of such plutons, some authors suggest a deeper and larger heat source triggered by large-scale tectonic processes such as subduction (Kaya, 2015; Gessner *et al.*, 2017; Roche *et al.*, submitted). In that sense, Kaya (2015) invoked a possible lithospheric thinning as the origin of the anomalously high heat flow. This example show that large-scale processes related to lithosphere dynamics could be involved in the genesis of geothermal systems. We thus need to employ a multi-scale approach (lithospheric- and crustal-scales), to improve the characterization of heat transfer possesses from the mantle to the geothermal system.

3. 3-D THERMAL EVOLUTION OF SUBDUCTION

In a previous study dedicated to the analysis of surface deformation in the Aegean-Anatolian domain, Sternai *et al.* (2014) found that mantle flow due to slab rollback and tearing can drag the upper plate from below, and explain upper plate extension and the formation of the North Anatolian Fault. Their results emphasize the active role of mantle flow in driving the surface strain and horizontal crustal velocities. However, the associated thermal processes were not described by these authors. Because heat transport is inherently coupled with deformation, mantle shearing may provide a strong heat source. Thus, we must consider it, especially if we want to describe in detail the thermal features associated with 3-D subduction dynamics when slab rollback and tearing occur. Indeed, while radioactive heat production is considered as the main heat source in the continental crust, shear heating has been suggested to be important in the mantle (Shubert and Yuen, 1978) and thus probably also in arc and back-arc settings where fast slab dynamics may be associated with intense asthenospheric flow. Here, we perform similar numerical simulations than Sternai *et al.* (2014), but improve the analysis by investigating the effects of shear heating. We describe the numerical results from a thermal point of view, by focusing on the localization of crustal thermal anomalies in the overriding plate.

3.1. Model setup

The numerical simulations were performed with the code "I3ELVIS" (Gerya, 2010) that solves the momentum, continuity and energy equations based on a staggered finite difference scheme combined with a marker-in-cell technique. Realistic, non-Newtonian visco-plastic rheologies are used in the model, and includes temperature- and pressure-dependent viscosities (see Appendix 2). The model setup is shown in Figure 3. The model domain measures

2000 x 328 x 1000 km in the x, y and z dimensions, respectively and is resolved by 501 x 165 x 197 grid points resulting in a resolution of 4, 2 and 5 km in the x, y and z dimensions, respectively. It includes three continental plates (C1, C2 and C3), allowing reproduction of similar tectonic events that affected the Tethys convergent domains (subduction, collision, slab tearing, trench retreat; Sternai *et al.* 2014). These three continental plates are defined by a crust of 35 km, 50 km and 45 km thick (Fig. 3). In addition to the trench-parallel weak fracture zone allowing for subduction initiation, the model includes a trench perpendicular weak fracture zone within the oceanic domain, which allows for slab tearing (Fig. 3).

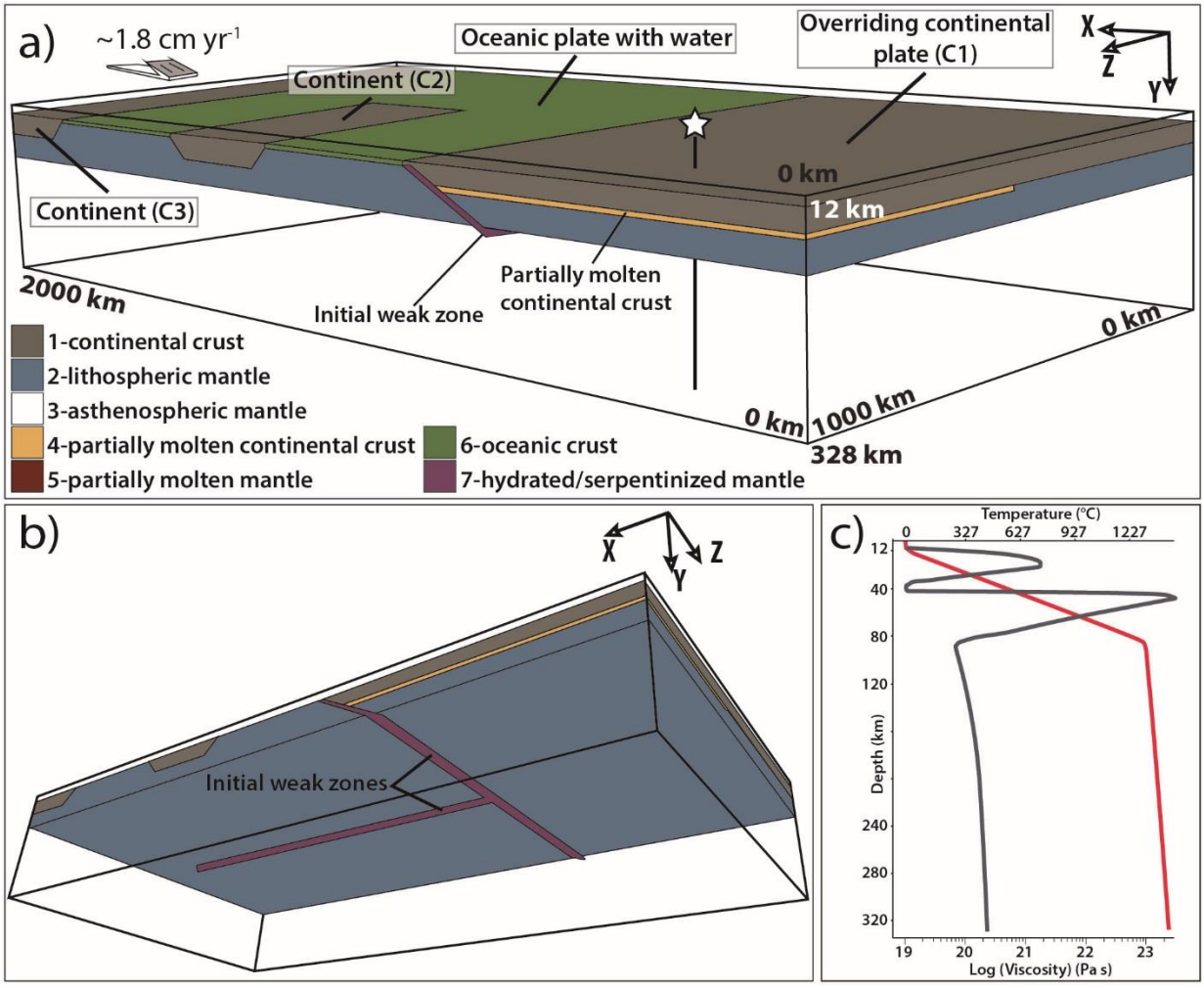

Figure 3: Numerical setup. (a) 3D initial model setup where the top layer ("sticky air", y < ~ 12 km") and the water are cut off for clarity. Colours showing different rock types. (b) Location of

the "weak zones" (i.e. hydrated/serpentinized mantle) into the lithosphere to trigger subduction (z-parallel) and to allow slab tearing (x-parallel) in the initial model. (c) Initial vertical profiles of viscosity (grey) and temperature (red), taken at the location shown by the white star.

The initial thermal structure of C1, C2 and C3 is laterally uniform with 0 °C at the surface and 1300 °C at 90, 140 and 150 km depth, respectively. The initial thermal structure of the oceanic lithosphere corresponds to the cooling age of 120 Ma (e.g. Turcotte and Schubert 2002). The initial temperature gradient in the asthenospheric mantle is ~ 0.5 °C km^{-1} (adiabatic). Boundary conditions involve free slip on the z = 0 and z = 1000 km sides of the model domain, while uniform and constant x-parallel velocities equal to ~ 1.8 cm yr^{-1} (convergence) are imposed at the x = 2000 km boundary, and the x = 0 km is fixed. Global mass conservation is ensured by material outflow through the permeable lower boundary (y = 328 km). Surface processes are also implemented using a highly simplified gross-scale erosion-sedimentation law. The parametric study on various boundary conditions and parameters is presented in Sternai *et al.* (2014).

Heat production by viscous or plastic shearing (H_s), consisting of the dissipation of the mechanical energy during irreversible non-elastic deformation, is controlled by the deviatoric stresses σ'_{ij} and strain rates $\dot{\varepsilon}'_{ij}$, as follow (Gerya, 2010):

$$H_s = \sigma'_{ij}\,\dot{\varepsilon}'_{ij} \quad (1)$$

The possibility to investigate H_s in our numerical simulations is a significant advance with respect to the previous models presented in Sternai *et al.* (2014). In order to test the possibility that slab tearing would enhance mantle shear heating, two series of numerical models, with and without slab tearing, have been performed, all other settings being equal (i.e. same boundary conditions, material properties, see more information in Appendix 2).

3.2. Results

Before focusing on thermal effects associated with slab dynamics, we briefly present the model evolution. The overall sequence of events is robust and includes first an early subduction of the oceanic domain between C1 and C2 with localized extensional deformation in the overriding plate. In our models, it includes the magmatic arc and the back-arc domain (see video S1 in Appendix 1). During this first subduction event, a toroidal mantle flow occurs below C1, as induced by the down-going slab. This event also controls crustal flow and surface deformation. Afterward, continental collision between C1 and C2 occurs, locally increasing slab dip and thus favoring slab tearing. Later subduction of the oceanic domain between C1 and C3 induces widespread extensional deformation in the overriding plate. This last event is highly conditioned by the previous horizontal to sub-horizontal return flow of hot asthenosphere, which warms up the incipiently subducting lithosphere close to the slab tear, enhancing here a non-cylindrical (i.e. not parallel to the initial upper plate margin) slab rollback. Rheological stratification of the upper plate is characterized at this stage by a thin rigid lithospheric mantle (~ 10 km). Deformation is localized in the overriding plate with strike-slip deformation propagating toward the subducting plate (Sternai *et al.*, 2014).

3.2.1. Thermo-mechanical instabilities

The early subduction event is characterized by the development of several positive thermal anomalies (i.e. anomalously high temperatures) (i) at the base of the crust with wavelengths around 200 km, and (ii) in the overriding lower crust, within a partially molten low-viscosity layer, with wavelengths around 30 km (Figs. 4a and 4b). The thermal instabilities in the low-viscosity crust generate dome-like structures cored by partially molten low-viscosity

material (orange colour in Figs. 4a and 4b). These domes are elongated parallel to the subduction trench and separated by 200 – 300 km (Fig. 4a). With time, new thermal domes appear toward the trench, controlled by the flow of low viscosity material in response to both slab rollback and tearing (Fig. 4b; Videos S2-S3 in Appendix 1). The strain rate distribution shows that mature crustal domes preferentially localize deformation, rather than incipient crustal domes closer to the trench (Fig. 4c). In addition, deformation localizes around the edges of these domes, showing the importance of lateral crustal strength contrasts on strain localization (Video S4 in Appendix 1). At 14.8 Myr, two domes have disappeared but the thickness of the partially molten layer at the base of the crust has tripled (from ~ 4 km to 15 km thick, Fig. 4b; Video S3 in Appendix 1). Meanwhile, the horizontal component of flow velocity in the partially molten layer has decreased (from ~ 5 to ~ 1 cm yr^{-1}, Fig. 4c). On the opposite, above the slab tear, the deformation is localized (see Fig. 4b in Sternai et al. (2014)) and horizontal component of crustal and mantle velocities have increased up to ~ 6 and ~ 9 cm yr^{-1}, respectively. The shear heating and the advective mantle heat flow components near the fast velocity zones are enhanced accordingly, as detailed below.

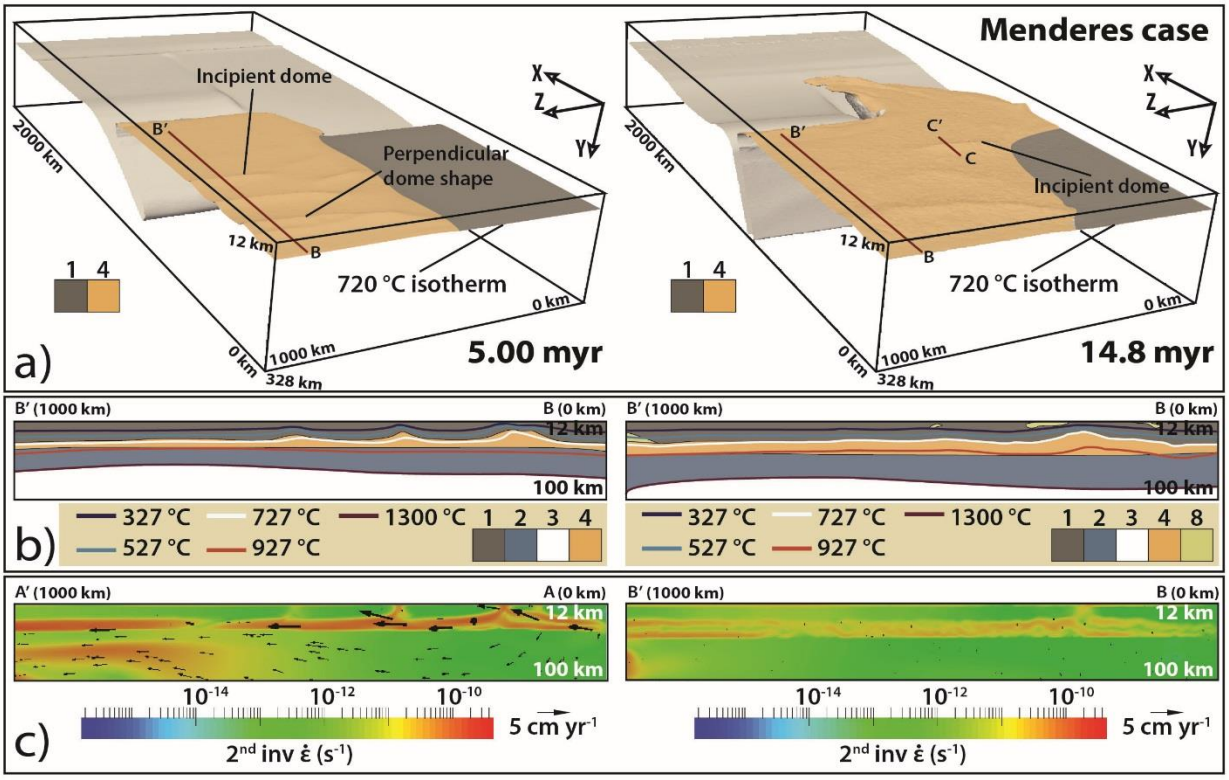

Figure 4: Thermo-mechanical evolution of the model. (a) The 720 °C isotherm at 5 myr and at 14.8 myr, respectively. Colours showing different rock types: 1, 4 indicate upper and lower crust, respectively, see also Figure 3. Note the position of CC' that may correspond to the 2-D numerical model cross-section. (b) Vertical cross-sections showing different rock types and isotherms. Colours showing different rock types: 1-2-3-4 as defined in Figure 3; 8-hydrated crust. (c) Vertical cross-sections showing the second invariant of the strain rate tensor and velocity vectors.

3.2.2. Slab dynamics and shear heating

The contribution of shear heating to heat production in our reference model (with slab tearing between C2 and the oceanic domain) is compared to similar simulations without slab tearing (Fig. 5; see Fig. S3 in Appendix 1). The frictional heat produced in the overriding plate locally reaches values of ~ 5.0 μW m^{-3} regardless of slab tearing (Fig. 5). However, when slab tearing occurs, a larger-scale thermal perturbation appears and develops below and at the base of the crust (~ 400 x 200 km at 12.4 Myr; see Fig. 5b). Anomalies associated with shear heating are

thus distributed over a larger domain in the case of tearing because of a more widespread mantle flow around the tear, and appear more localized and parallel to the subduction trench without tearing (Fig. 5a, see right panel). In addition, our results show that the amount of heat produced by shearing leads to an increase of mantle heat flow (Q_m) at the base of the crust, and particularly above the tear. In particular, for average shear heating of ~ 2.0 μW m^{-3} and mantle thickness of 30 km (Fig. 5c, profile 1), the contribution to the heat flow nearby the subduction front is of ~ 60 mW m^{-2} at 12.4 Myr. Conversely, far from the subduction front, shear heating is insignificant (< 1.0 nW m^{-3}, see Fig. 5c, profile 4), implying no contribution of this mechanism to heat production by this mechanism (Fig. 5d, profile 1).

Shear heating in the mantle during slab retreat and tearing plays a key role in increasing temperatures at the base of the overriding crust, where mantle heat flow values are around 100 mW m^{-2} and reach locally up to 130 mW m^{-2} above the slab tear at 12.4 Myr (Fig. 5b, see left panels). We found that 46 % of the heat flow at the base of the crust is due to mantle shear heating, the remaining part being due to the advection of hot material. In the absence of slab tearing, the average of mantle heat flow at similar times is around 80 mW m^{-2}, reaching locally up to 155 mW m^{-2} but over a much smaller area, (Fig. 5b, right). We therefore suggest that advection of hot asthenosphere to shallow depths during slab retreat and tearing plays an important role in increasing temperatures at the base of the crust (Fig. 6). Furthermore, mantle heat flow values may reach steady-state after ~ 4 Myr (values around 40 – 50 mW m^{-2}, Fig. 5d).

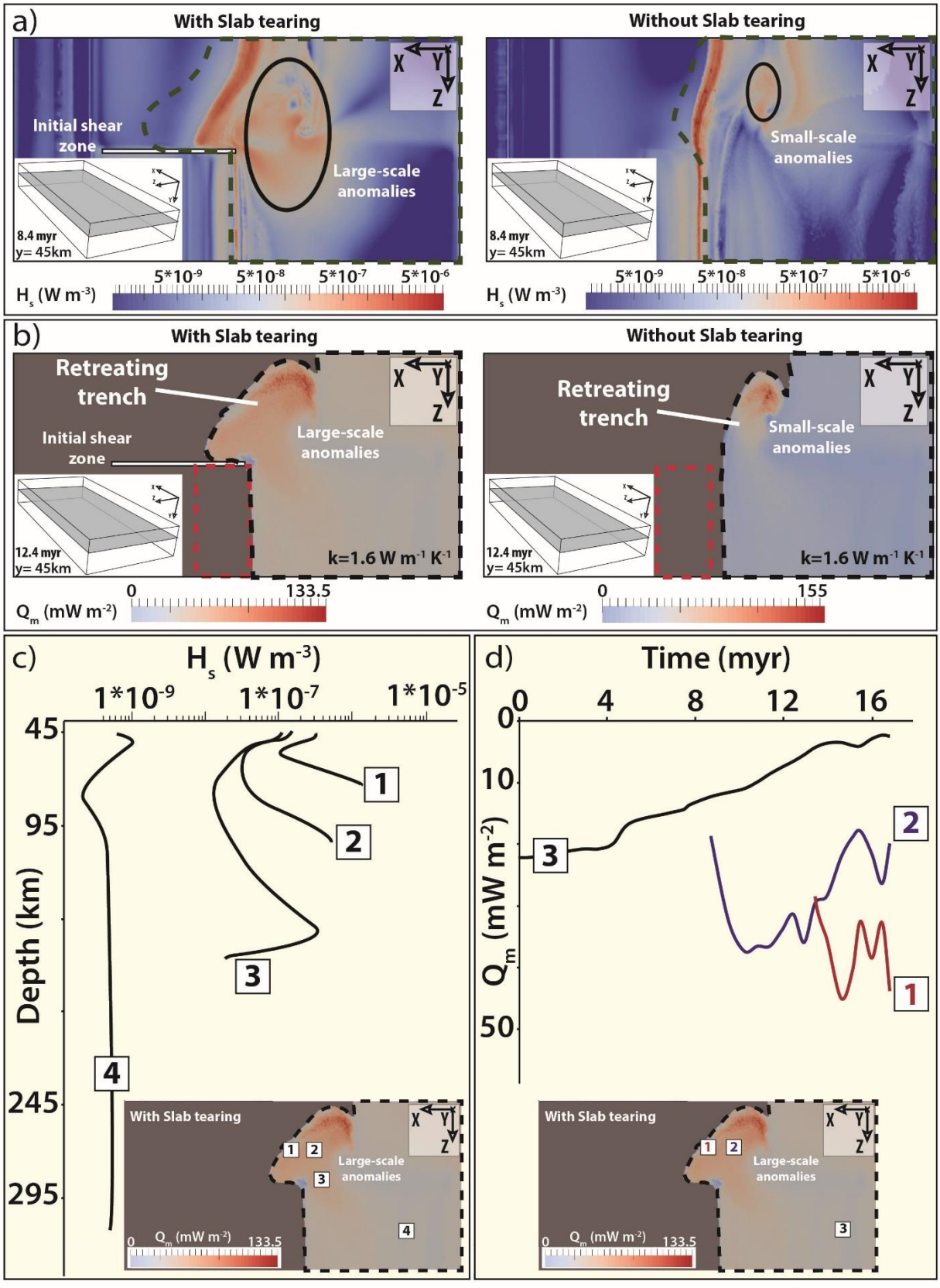

Figure 5: Mantle heat source with and without tearing at the mantle-crust transition. (a) Plan view

of shear heating (H_s) at the mantle-crust transition at 8.4 Myr. Dashed line on both panels shows the plan view of the overriding plate C1. (b) Plan view of mantle heat flow (Q_m) at the mantle-crust transition at 12.4 Myr. Black and red dashed lines on both panels show the plan view of the overriding mantle, and of the overriding C2, respectively. (c) Vertical depth-shear heating (H_s) profiles in the mantle below the stretched overriding plate at t_0 + 14.8 myr, taken at the location shown by the white squares. (d) Evolution of mantle heat flow (Q_m) at the mantle-crust transition. The values are taken at the location shown by the white squares.

To summarize, slab tearing facilitates the rollback of the subducting plate and extension within the upper plate. Consequently, slab tearing and its associated mantle flow contributes to the increase in heat flux at the base of the crust by (i) enhancing mantle shear heating and (ii) controlling the return flow of hot asthenosphere (e.g. toroidal and poloidal mantle flow components). Both mechanisms together appear to be able to increase the Moho temperature by up to 250 °C (Fig. 6). Therefore, slab tearing may (i) affect the heat source responsible for regional HT-LP metamorphic rocks in MCCs and (ii) explain regional high-temperature anomalies across amagmatic geothermal systems in post-subduction settings.

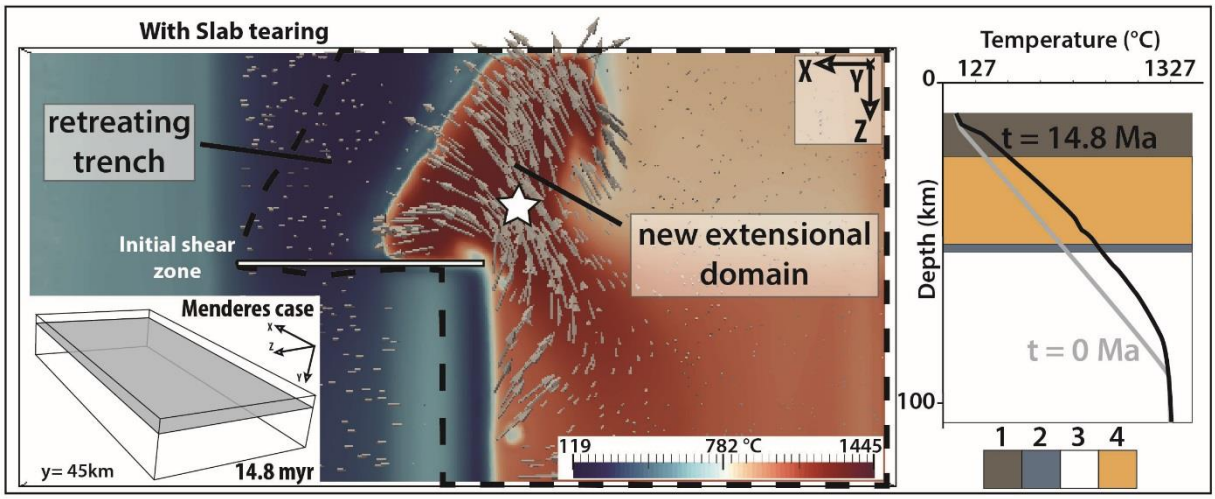

Figure 6: Plan view of temperature anomaly at the mantle-crust transition (~ 45 km depth) in the case of slab tearing. Grey arrows represent the velocity vectors in the asthenosphere. Black dashed line on the left panel shows the plan view of the overriding plate C1. Right panel: vertical temperature profiles at t_0 and t_0 + 14.8 myr, taken at the location shown by the white star. Colours showing different rock types: 1-2-3-4, as defined in Figure 3.

4. FROM SUBCRUSTAL THERMAL ANOMALIES TO GEOTHERMAL SYSTEMS: 2-D MODEL OF FLUID CIRCULATION

Results of the 3-D model show that at 12.4 Myr, mantle heat flow can reach anomalously high values exceeding 130 mW m^{-2} (Fig. 5b). At 10 km depth above the tearing, temperature values vary between 450 and 500 °C, and are thus similar to estimated temperatures from aeromagnetic data at the same depth in the Menderes Massif (~ 580 °C) (Aydin *et al.*, 2005). Using these results, we defined a 2-D fluid flow model in a porous media to analyse the thermal consequences of anomalously high basal heat flow on fluid circulation in the upper crust. The advantage of this model is a good spatial resolution (see Appendix 2), representative permeability, and realistic rock and fluid properties.

The model measures 120 x 10 km and is designed to represent a SSW-NNE cross section of the Menderes massif. We choose the basal heat flow in order to (1) account for previous 3-D numerical results where mantle heat flow could reach values up to 130 mW m^{-2} (Fig. 5b), and (2) reproduce temperatures above 500 °C at 10 km depth, as suggested by Curie-point depths in western Anatolia (Aydin *et al.*, 2005). The objective of this model is to understand the effects of high basal heat flux on the fluid flow circulation pattern, in particular around permeable detachments. In the following, we describe the main characteristics of the model setup and present the main results.

4.1. Model setup

Coupling between Darcy's law, heat transfer equation and mass conservation is performed using the Comsol Multiphysics™ software (finite element method). Details about the numerical procedure (benchmark experiments, model setup, fluid and rock properties) are given in Appendix 2. The model is shown in Figure 7, where two detachment faults (with a dip angle varying from 10 to 20°) represent the Büyük Menderes and the Alaşehir Menderes detachments (Fig. 2b). Figure 7a illustrates the mesh refinement in permeable zones (close to the surface and within the detachments). A convective flux condition was imposed at the top of the detachments, in order to allow the emergence of hot fluids at the surface. In addition, we use temperature-dependent density and viscosity laws for fluids (see Appendix 2). No magmatic source is present in the model, and the chosen basal heat flow value at a depth of 10 km corresponds to 120 mW m^{-2} (Fig. 7b). This value is therefore consistent with both criteria (i.e. mantle heat flow from our 3-D model and Curie-point depths estimations). A constant pressure of 10^5 Pa is imposed at the surface allowing fluid influx while no flow is allowed across the others boundaries of the box (Fig. 7b). At time t = 0, thermal regime is purely conductive (see white isotherms in Fig. 7c). Then, permeability values are switched on (color code of Figure 7c; Appendix 2) and the transient evolution of temperature and velocity fields are recorded during 5 Myr. Permeability in the basement (k_b) decreases exponentially with depth (Manning and Ingebritsen, 1999) (see Fig. 7c and Appendix 2) while detachment permeability is assumed constant (k_d). Despite a number of arguments in such extensional setting suggest high permeability at the surface (highly fractured and karstified rock, see Özen *et al*. (2012)) numerical values remain unconstrained. We therefore decided to test a wide range of realistic permeabilities for the basement (i.e. from 10^{-17} to 10^{-14} m^2) and the detachment fault with same range of values (Fig. 7b).

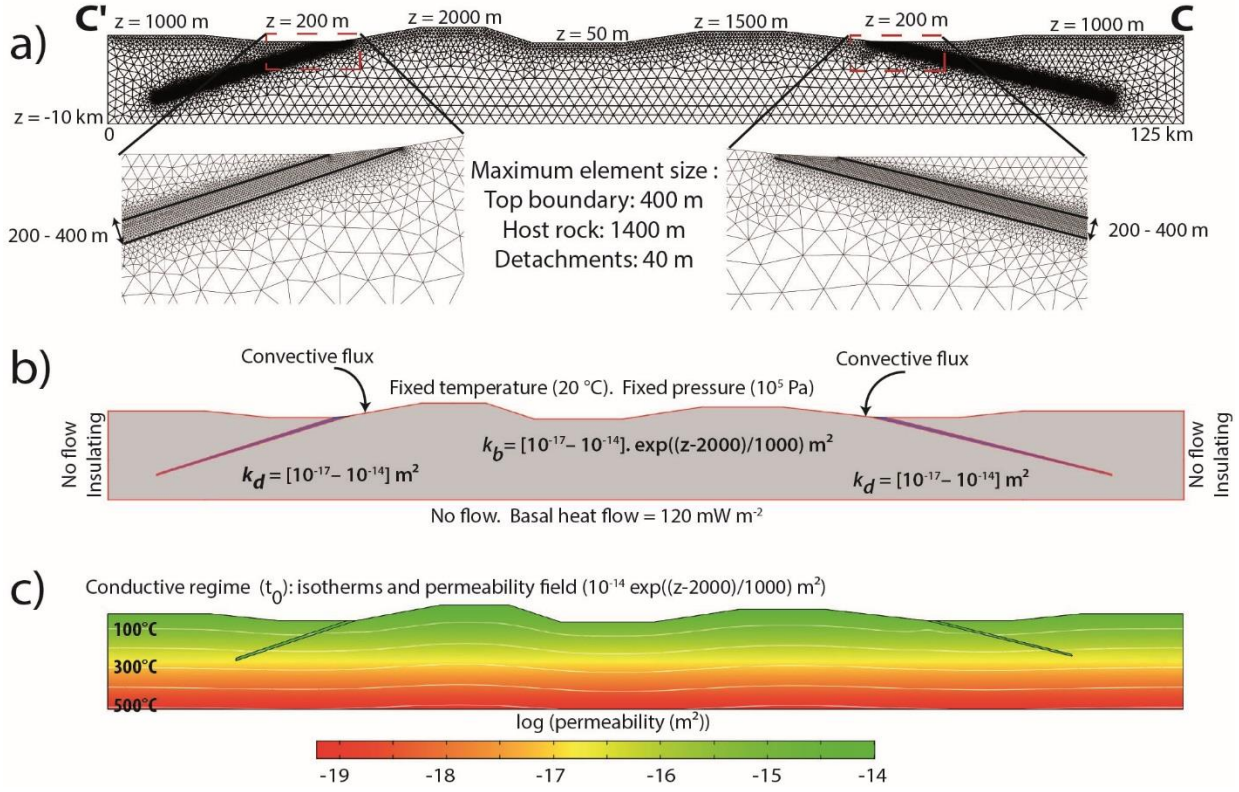

Figure 7: (a) Geometry and mesh used for 2-D models of fluid circulation in the upper crust of the Menderes area, where MCCs and detachments are reproduced. This cross section would correspond, from left to right, to a N-S cross section, from Salihli to Salavatlı geothermal areas. Mesh is refined at the top surface and within detachments, where permeability is the highest. (b) Boundary conditions and range of values for permeability (note the depth-dependence of the host rock permeability). (c) Steady-state conductive regime, where isotherms in white are separated by 100 °C. Colors refer to permeability values affected at time t > 0 (see text) for the case detailed in Figure 9.

4.2. Results

4.2.1. Role of basement and detachment permeabilities

Figure 8 illustrates steady-state temperature fields for different combinations of both basement and detachment permeability. In Figure 8a, results show the major role of k_b to distort

387 significantly the isotherms, even if k_d is high (10^{-14} m²). In the upper case of Figure 8a, isotherms
388 remain flat and no thermal reservoir forms beneath the detachments. Alternatively, the lower case
389 with realistic higher permeability values shows a general fluid circulation pattern characterized
390 by: (i) surface meteoric fluids that flow from topographic highs to the top of the detachment fault
391 and other topographic lows, inducing a negative thermal anomaly in the hanging walls of
392 detachments; (ii) at depth, hot fluids are drained upward by the permeable detachments allowing
393 for isotherms to rise along the fault zones (see uplifted isotherms in bottom case of Fig. 8a). A
394 positive thermal anomaly is due to hot fluids rising up toward the top of the detachment while a
395 negative thermal anomaly induced by topography-driven flow grows in the hanging walls of
396 detachments, leading to the formation of hot fluid reservoirs beneath the detachments (near the
397 surface). To synthetize, at the scale of the whole massif, thermal undulations mimicking dome-
398 like structures are localized beneath topographic lows in the case of a high basement permeability
399 (Fig. 8a, bottom case).

400

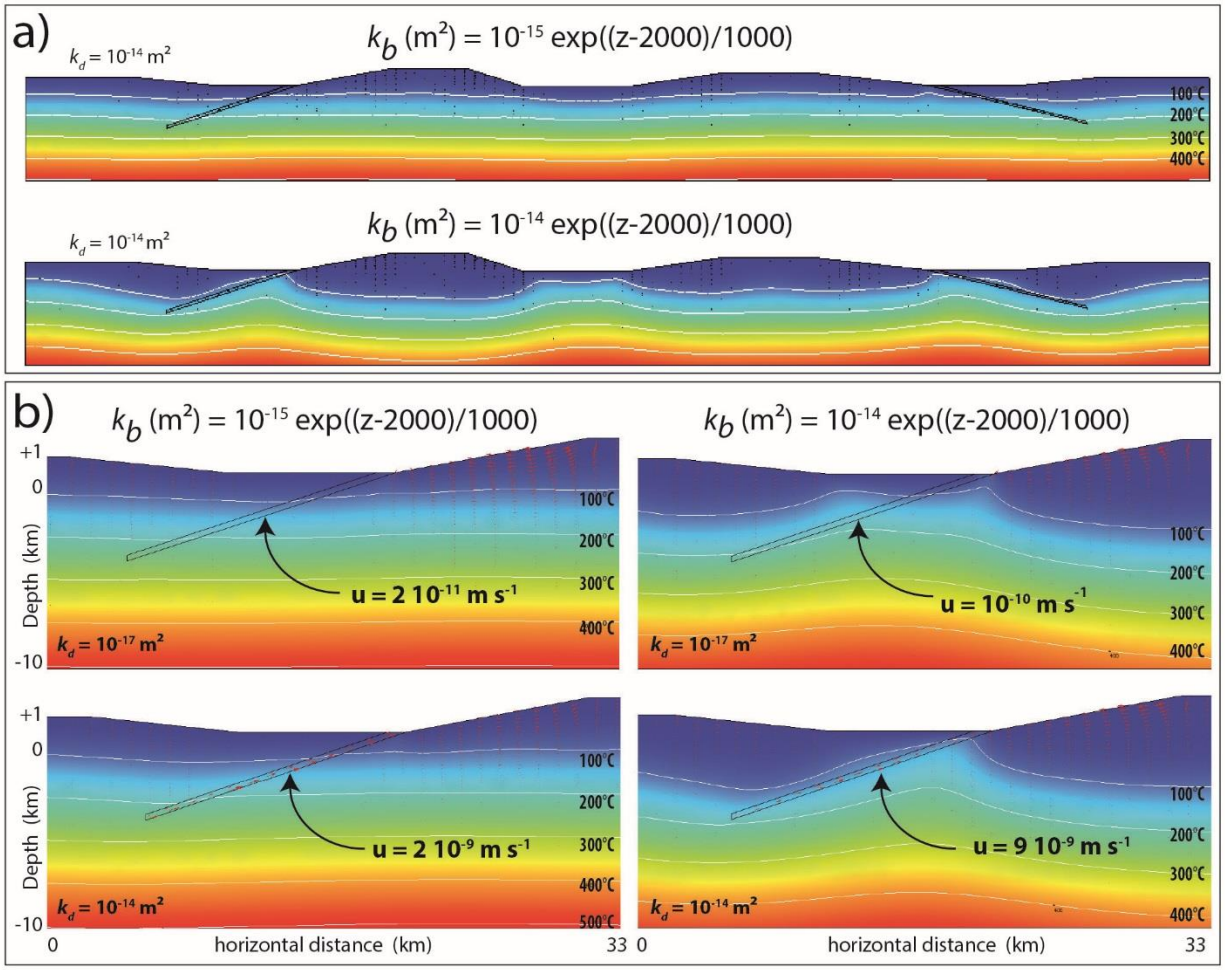

401

402 Figure 8: Results for thermal perturbations due to fluid circulation in permeable zones for varying
403 basement permeability (k_b) and for varying detachment permeability (k_d). (a) role of the basement
404 permeability for a fixed value of k_d (10^{-14} m²). (b) Zoom on the left detachment, with varying
405 permeabilities (small k_d value in the top row; high k_d value in the bottom row). Left (right) column
406 corresponds to a small (high) basement permeability.
407

408 When k_d is varied (Fig. 8b), it turns out that thermal reservoirs establish at shallow depth
409 when both k_d and maximum k_b values are important (10^{-14} m², bottom right case in Fig. 8b). In
410 the case where k_d is low (10^{-17} m², top case in Fig. 8b) two thermal reservoirs appear only with a
411 high maximum k_b value, suggesting that topography-driven flow is dominant. However,

412 temperatures at shallow depth and fluid velocity values within the detachment are much lower
413 than in the high k_d case (bottom right case in Fig. 8b). Crustal-scale permeable faults and their
414 induced high topography thus control the spatial distribution of upper-crust thermal anomalies at
415 depth, mimicking dome-like structures beneath topographic lows (Fig. 8a, bottom case, and Fig.
416 8b, right column).

417 ***4.2.2. Fluid flow field and temperature profiles***

418 Figure 9a illustrates the fluid flow velocity pattern in the case of Figure 8a (bottom case).
419 Fluid flow is favored by high-topography and permeable zones such as detachments. Located
420 within detachments, high velocity areas (> 10^{-10} m / s – or 0.32 cm / yr) are recorded down to 5
421 km deep (red areas). The bottom panel of Figure 9a shows a horizontal temperature profile at 1
422 km depth. It is important to note that temperature anomalies of ~ 140 °C are focused close to the
423 top of the detachments. Figure 9b (left column) shows computed vertical temperature profiles at
424 different distances from the two detachments, at a given time (i.e. 4 x 10^4 yr). Figure 9b (right
425 column) illustrates temperature measurements at the Aydin-Salavatlı geothermal field, Büyük
426 Menderes Graben, within 2 boreholes ~1.5 km apart. Although the comparison of daily-measured
427 thermal profiles with these two sets of vertical temperature profiles is limited, one can observe
428 some similarities with (i) a high-temperature gradient at the surface, decreasing rapidly with
429 depth, and (ii) some negative values of the temperature gradient. In addition, modeled
430 temperatures are comparable, with emergence temperatures around 60 °C and reservoir
431 temperatures at depth around 180 – 200 °C. Because our density law is simplified (see Appendix
432 2), and because the vapour phase is not accounted for, the computed profiles show rather smooth
433 curves when compared to measurements. However, the typical convective signatures in
434 temperature profiles are similar.

435

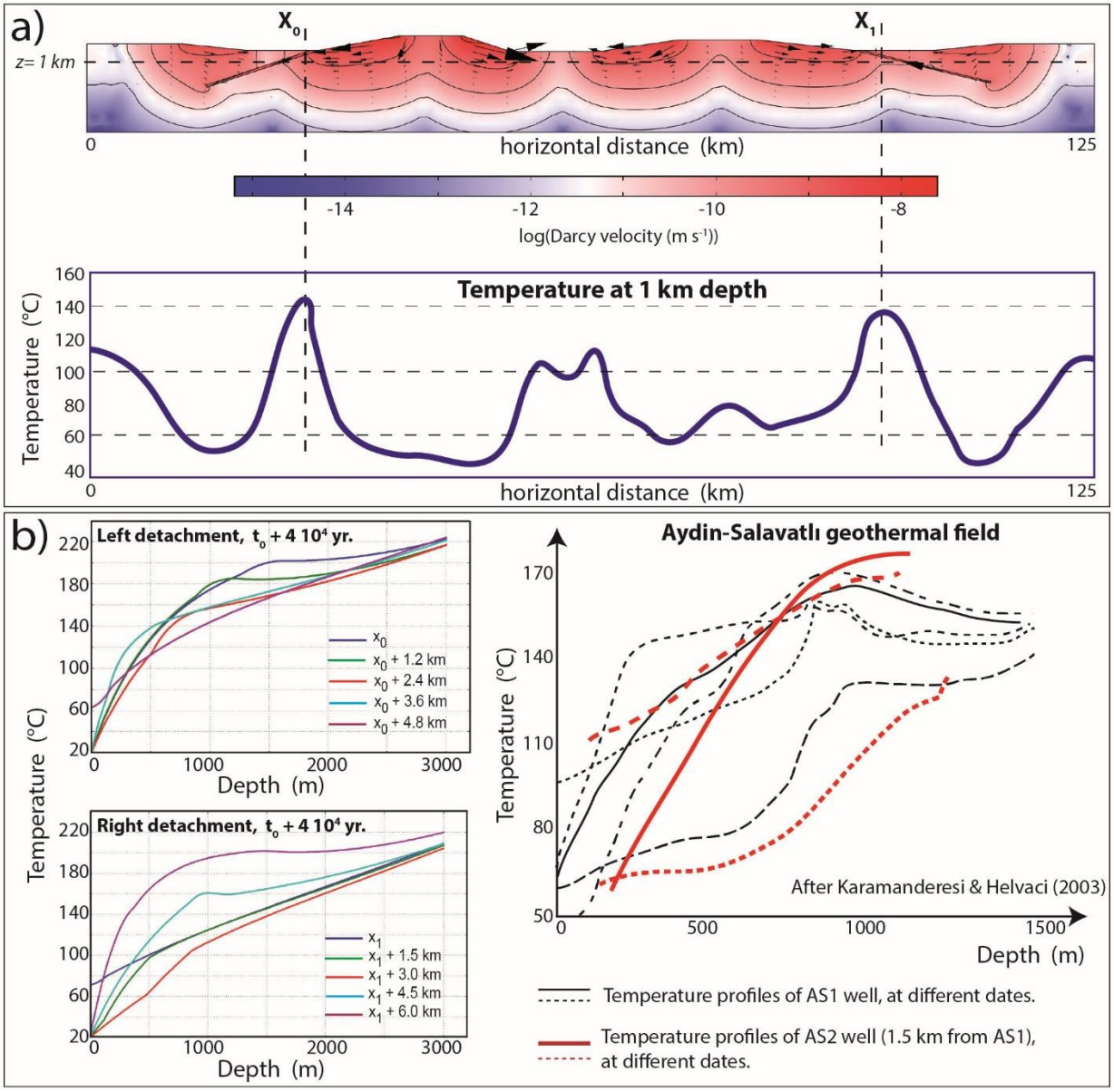

436

437 Figure 9: Results for the experiment shown in the lower case of Figure 8a (and right case of
438 Figure 8b). (a) Fluid flow velocity field (colors, isocontours and arrows) and horizontal
439 temperature profile at 1 km depth (dashed line in the fluid flow pattern). Note that the largest
440 temperature perturbations correspond to the top of the detachment locations (x_0 and x_1). (b)
441 Computed vertical temperature profiles at time $t_0 + 4\ 10^4$ yr. x0 and x1 are indicated in Figure 9a.
442 On the right, measured temperature profiles at the Aydin-Salavatlı geothermal field; black curves

(plain and dashed) correspond to different measures in the same AS1 borehole (different dates of measurements) and red lines are measured in the AS2 borehole, 1.5 km from the AS1 borehole (after Karamanderesi and Helvaci, 2003).

5. DISCUSSION

5.1. Large-scale thermo-mechanical boudinage, and emplacement of MCC in Western Anatolia

The modeled thermo-mechanical instabilities (Fig. 4) are not only analogous to crustal and lithospheric boudinage (Ricard and Froidevaux, 1986), but they add a thermal component to what was generally assumed to be purely mechanical. These instabilities developed in the overriding plate are triggered by both shear heating and hot mantle flows. These mechanisms indeed induce a thermal weakening of the lithosphere, thus controlling the development of boudinage at different scales, and the localization of MCCs in the extensional crust. It is important to note that these domes are also promoted by the low-viscosity crust, which is related to the chosen initial thermal regime in our models. When the slab tear is accounted for, the crust is weak over a wider domain above the tear, increasing its ability to flow (e.g. Block and Royden, 1990; Rey *et al.*, 2009) and to form HT domes. In other words, shear heating and mantle flow control the position of positive thermal anomalies in the overriding crust, which, in turn, control the deformation pattern in the lower crust during extension. Such a lithospheric thermal weakening is further enhanced by the accumulation of magmas in the back-arc domain, which is widely promoted by slab rollback and tearing processes (Menant *et al.*, 2016b).

In the Cyclades (Greece), the dominant wavelength of MCCs (several tens of kilometres, similar to the spacing between the different islands) is compatible with that expected for crustal-scale boudinage (Fig. 4). At the scale of the whole Aegean domain, long-wavelength variations

of Moho depth (Tirel *et al.*, 2004; Karabulut *et al.*, 2013) are more reminiscent of lithospheric-scale boudinage (several hundreds of km; Fig. 4). This boudinage of the crust induces migmatite-cored MCCs which were first exhumed in the northern Menderes Massif in the Micoene (Cenki-Tok *et al.*, 2016), and then in the central and eastern Cyclades since the lower Miocene (Jolivet *et al.*, 2015), coevally with a further acceleration of trench retreat related to the Hellenic slab tearing. This is consistent with our model, where dome-like structures, cored by partially molten low-viscosity material, develop first in the overriding plate, and then migrate toward the trench, in response to both slab rollback and tearing (Figs. 4a and 4b). In addition, we suggest also that excess heat due to these subduction dynamics controlled the retrogression in the greenschist-facies of high-pressure metamorphic rocks in Cyclades (post-orogenic extension), consistently with acceleration of slab retreat around 35 Ma (Jolivet *et al.*, 2015). Furthermore, our numerical experiments highlight an increase of Moho temperature during a few Myrs related to asthenosphere upwelling below the overriding plate (Figs. 5d and 6). We therefore suggest a similar heating for the mantle-crust boundary in the Anatolian-Aegean domain, which is consistent with the presence of HT metamorphic domes and the formation of syn-extension granites and migmatites throughout the entire western Anatolian-Aegean domain between 20 Ma and 8 Ma (Jolivet *et al.*, 2015; Menant *et al.*, 2016a).

In the Menderes MCC (located above the slab tear, see Fig. 2), strain was first localized in the north, along the Simav Detachment (early Miocene, stage 1 after Gessner *et al.* 2013) accommodating the exhumation of an asymmetric migmatite-cored MCC (Rey *et al.*, 2009; Cenki-Tok *et al.*, 2016). Then, strain migrated southward, toward the trench and localized within the central part of the Menderes Massif (Fig. 2c). The Alaşehir and Büyük Menderes detachments assisted exhumation of the lower crust during slab tearing (middle-late Miocene, stage 2 after

490 Gessner *et al.* 2013). This implies that the central part of the Menderes Massif had become weaker
491 than the previously activated Simav area, probably due to the extra source of heat associated with
492 slab tearing. According to Labrousse *et al.* (2016), the evolution of the style of extension from an
493 asymmetric MCC (localized deformation, case of the Simav detachment) to a double-dome
494 symmetric MCC (distributed deformation, case of the Menderes detachments) implies that heat
495 input at the base of the crust is higher than heat dissipation due to stretching. These observations
496 are consistent with the thermal features observed in our model, which emphasize the crucial role
497 of shear heating, as well as poloidal and toroidal components of mantle flow, to heat the lower
498 crust (Figs. 5 and 6). Both mechanisms are thus responsible for the presence of large-scale
499 thermal anomalies at depth (i.e. 580 °C at 10 km depth) and at the surface (i.e. heat flow values
500 around 100 mW m^{-2}, Erkan, 2015). As a consequence, the thermal state of the crust induced by
501 elevated mantle heat flow could control the style of extension (asymmetric versus symmetric
502 MCC).

503 Furthermore, hot fluids circulating within crustal-scale permeable faults help increasing
504 basal temperatures (around the ductile/brittle transitions) by several tens of °C (Fig. 8a), resulting
505 in a positive feedback for the formation of new shear zones and MCCs at depth. In this case,
506 magmatic bodies such as granitoids and migmatites may be developed and localized below the
507 detachment, as it seems to be the case in the Menderes with the Salihli diorite and Simav granites.

508 The progressive formation of HT domes topped with extensional detachments can thus
509 be summarized as follows: (1) mechanical (boudinage) and thermal instabilities within the
510 stretched lithosphere generate a series of domes, periodically spaced, producing rheological
511 heterogeneities (i.e. low-viscosity layers) that are likely to localize extensional shearing
512 deformation on their edges (Le Pourhiet *et al.*, 2003; Huet *et al.*, 2011) and (2) upward flow of

513 deep hot fluids and downward flow of cold surface fluids further increase thermal contrasts across
514 the shear zones, enhancing the localization of deformation.
515
516 **5.2. Detachments and localisation of HEGRs in Western Anatolia**
517 The relationships between the localization of the deformation and thermal domes (Fig. 4)
518 are similar to that documented in MCCs, and may be associated with crustal-scale permeable
519 faults, which can provide pathways for meteoric waters to flow into the actively deforming
520 middle crust (e.g. Famin *et al.*, 2005; Mulch *et al.*, 2006). As shown in Figure 5, the excess of
521 mantle heat flow is transfered by conduction into the crust, affecting the fluids present in the
522 crustal porosity. These fluids may then undergo deformation-driven flow in ductile shear zones
523 (e.g. Oliver, 1996), but also thermally driven (i.e. buoyancy-driven) flow through the crust, where
524 high permeability detachments may easily collect and bring up deep hot fluids. Indeed, our 2-D
525 numerical models suggest that an elevated basal temperature (580 °C) at 10 km depth would
526 induce temperatures of 300 – 350 °C at a depth of 6 km and thus a sufficiently high fluid density
527 contrast to permit upward flow along the low-angle fault in the shallower crust. In that case,
528 buoyancy-driven flow is superimposed to topography-driven flow (Fig. 8). In other words, the
529 topography-driven flow, which prevails in the regional fluid flow pattern, is dominated by
530 buoyancy-driven flow within highly permeable detachments.
531 Although the spatiotemporal evolution of permeability within detachments is poorly
532 known, field observations on these geological structures (Famin *et al.*, 2005) suggest that they
533 could represent highly permeable zones of several hundreds of meters thick where fluid flow is
534 facilitated (Fig. 10). Moreover, if these channelized fluid flow systems are tectonically active,
535 earthquake faulting may be associated with seismic pumping that enhances fluid migration

toward dilation zones (Sibson *et al.*, 1975; Famin *et al.*, 2005). As a consequence, detachments may be considered as the crustal-scale structural control for the circulation of deep geothermal fluids related to HEGRs (e.g. Bellani *et al.*, 2004; Roche *et al.* submitted), driving the long-term crustal-scale history of the geothermal systems (Fig. 10). However, it is noteworthy that most of the geothermal systems in the Menderes Massif reside in fault intersection zones, where N-S transfer faults and low-angle normal faults mostly formed dilational jogs that seem to promote the emergence of hot waters and gas vents (Roche *et al.*, submitted). Fault interactions would thus allow for fluid rising in the hanging wall from the reservoirs located below the detachment (Fig. 8b, right column), and control the location of thermal springs. Further numerical simulations would therefore be required to confirm this hypothesis based on field observations.

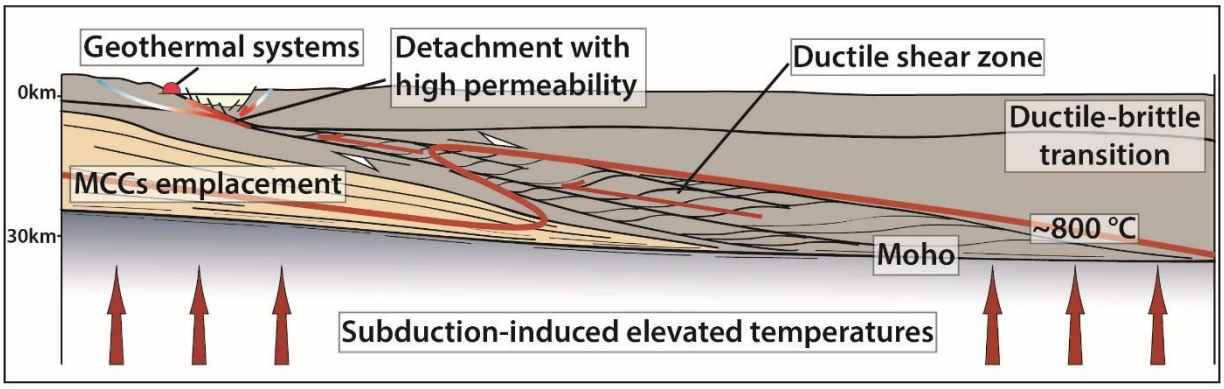

Figure 10: Schematic cross section showing fluid flow associated with detachment zone in back-arc area. Red arrows indicate fluid circulation in ductile crust and circulation of meteoric fluids in the upper crust are underlined by colored pathways (blue for cold and red for warm).

5.3. Subduction dynamics and localisation of HERSs: the Larderello (Tuscany) and the Basin and Range (Western United States) areas

Our 3-D and 2-D model results are relevant to other regions, and thus may explain relationships between subduction dynamics and the location of geothermal provinces; for instance, (i) in the Larderello area post-orogenic extension is active in back-arc domain; or (ii) in the Basin and Range Province (western United States). In both cases, MCCs are exhumed along low-angle normal faults, and therefore represent a favorable setting for HEGRs. While some of them are considered as "amagmatic" in origin (e.g. Bellani *et al.*, 2004; Faulds *et al.*, 2010), some authors require a magmatic heat source (e.g. Koenig and McNitt, 1983; Santilano *et al.* 2015). Through these two main additional examples, we show that the "magmatic" vs. "amagmatic" classification may be ambiguous according to the long-term behavior of these geothermal systems.

In the Northern Tyrrhenian Sea and Tuscany regions, subduction dynamics has also been controlled by slab retreat since the Oligo-Miocene. This region is characterized by a shallow Moho discontinuity (20 – 25 km depth), and a reduced lithosphere thickness due to uprising asthenosphere and the delamination of crustal lithosphere (Gianelli, 2008). At crustal-scale a series of low-angle normal faults crosscut the old thrusts (e.g. Faccenna *et al.*, 1997; Jolivet *et al.*, 1998), and thus cannot be explained by a reactivation of pre-existing inherited discontinuities. Instead, our numerical models suggest that thermo-mechanical boudinage induced by slab rollback triggers the formation of localized shear zones and allows the exhumation of MCCs (e.g. Elba Islands, Fig. S4 in Appendix 1). These shear zones are still active (Bellani *et al.*, 2004) and may control the ascent of magmatic intrusions, such as beneath the Larderello geothermal field.

We therefore suggest that magmatic intrusions in the upper crust result directly from the deep thermal anomaly associated with slab dynamics during extension.

Although subduction dynamics are quite different in the Basin and Range province (i.e. first characterized by slab retreat since the Eocene at the northern edge of the Farallon slab (Schellart *et al.*, 2010), and then by an asthenospheric upwelling above the Californian slab window at 30 Ma (Atwater, 1970)), similar remarks also hold for this region. Indeed, our results are consistent with geological observations where the presence of a conductor at 15 – 35 km depth range (Wannamaker *et al.*, 2008) suggests that the central part of the Basin and Range domain has become weaker, probably due to an extra source of heat associated with slab window (i.e. magma underplating due to mantle flow and shear heating). In light of our numerical results, we propose that fast-flowing asthenosphere also strongly heats the lithospheric mantle and the lower crust via shear heating and mantle upwelling processes. Lithospheric weakening thus promotes the propagation of major fault zones throughout the crust, leading to the connection between the weaker conductive lower crust and the brittle upper crust (Fig. 10). Hot thermal fluids at depth can then ascend within the damage fault zones, which thus control the location of HEGRs at the surface (Faulds *et al*., 2010). It is noteworthy that the presence of recent intrusions (e.g. Steam Boat, Casa Diablo in the Walker Lane geothermal belt, Koenig and McNitt, 1983) locally enhances thermally-driven flow, by increasing the temperatures of the geothermal systems but this seems marginal as little active volcanism is recognized in this region (Faulds *et al*., 2010).

6. CONCLUSIONS

3-D numerical experiments show that the mantle flow and shear heating resulting from slab retreat and tearing have a significant effect on Moho temperatures during 5 – 10 Myrs. Such a mechanism induces lithospheric and crustal thermal boudinage with different wavelengths, which in turn creates thermally-driven rheological contrasts that localize deformation and lead to the formation of crustal-scale permeable detachments. These structures allow for the exhumation of MCCs and for the emplacement of HEGRs comparable to those observed in the Mediterranean realm and in the Western United States. Although there is no consensus on a worldwide classification of geothermal systems, our results highlight the importance of the spatial and temporal scales of subduction dynamics in the control of genesis of geothermal systems.

ACKNOWLEDGMENTS

This work has been financially supported by the LABEX VOLTAIRE (ANR-10-LABX-100-01) of the University of Orléans and by the French Geological Survey (BRGM). This paper is a contribution of the ERC RHEOLITH Project (ERC advanced grant no. 290864). Pietro Sternai is grateful to the Swiss NSF Ambizione grant PZ00P2_168113/1. Numerical simulations were performed on the ETH-Zürich clusters BRUTUS and EULER. The paper benefited from relevant revisions by David Whipp and one anonymous reviewer.

REFERENCES

Aydın, İ., Karat, H. İ., and A., Koçak. (2005), Curie-point depth map of Turkey. Geophysical Journal International, 162(2), 633-640.

Bertani, R. (2016), Geothermal power generation in the world 2010–2014 update report. Geothermics, 60, 31-43.

Bellani, S., Brogi, A., Lazzarotto, A., Liotta, D., and G., Ranalli. (2004), Heat flow, deep temperatures and extensional structures in the Larderello Geothermal Field (Italy): constraints on geothermal fluid flow: Journal of Volcanology and Geothermal Research, 132(1), 15-29.

Blackwell, D. D., Smith, R. P., Waibel, A., Richards, M. C., and P., Step. (2009). Why Basin and Range systems are hard to find II: Structural model of the producing geothermal system in Dixie Valley, Nevada. Geothermal Resources Council Transactions, 33, 441-446.

Block, L., and L.H., Royden. (1990), Core complex geometries and regional scale flow in the lower crust: Tectonics 9, 557–567.

Bousquet, R., Goffe, B., Henry, P., LePichon, X., and C., Chopin. (1997), Kinematic, thermal and petrological model of the Central Alps: lepontine metamorphism in the upper crust and eclogitisation of the lower crust: Tectonophysics 273, 105–127.

Bozkurt, E., Satır, M., and Ç., Buğdaycıoğlu. (2011), Surprisingly young Rb/Sr ages from the Simav extensional detachment fault zone, northern Menderes Massif, Turkey. Journal of geodynamics, 52(5), 406-431.

Brogi, A., Capezzuoli, E., Martini, I., Picozzi, M., and F., Sandrelli. (2014), Late Quaternary tectonics in the inner Northern Apennines (Siena Basin, southern Tuscany, Italy) and their seismotectonic implication. Journal of Geodynamics: 76, 25-45.

637 Cenki-Tok, B., Expert, M., Işık, V., Candan, O., Monié, P., and O., Bruguier. (2016), Complete
638 Alpine reworking of the northern Menderes Massif, western Turkey: International Journal
639 of Earth Sciences, 105(5), 1507-1524.
640 Cumming, W. (2009), Geothermal resource conceptual models using surface exploration data.
641 In Proceedings.
642 De Boorder, H., Spakman, W., White, S. H., and M. J. R., Wortel. (1998), Late Cenozoic
643 mineralization, orogenic collapse and slab detachment in the European Alpine Belt. Earth
644 and Planetary Science Letters, 164(3), 569-575.
645 Erkan, K. (2015), Geothermal investigations in western Anatolia using equilibrium
646 temperatures from shallow boreholes. Solid Earth, 6(1), 103.
647 Faccenna, C., Mattei, M., Funiciello, R. and L., Jolivet. (1997), Styles of back-arc extension in
648 the Central Mediterranean: Terra Nova, 9, 126-130.
649 Famin, V., Philippot, P., Jolivet, L., and P., Agard. (2004), Evolution of hydrothermal regime
650 along a crustal shear zone, Tinos Island, Greece. Tectonics, 23(5).
651 Faulds, J., Coolbaugh, M., Bouchot, V., Moek, I., & Oguz, K. (2010). Characterizing structural
652 controls of geothermal reservoirs in the Great Basin, USA, and Western Turkey:
653 Developing successful exploration strategies in extended terranes. In World Geothermal
654 Congress 2010 (pp. 11-p).
655 Gerya, T. (2010), Introduction to Numerical Geodynamic Modelling: Cambridge University
656 Press.
657 Gessner, K., Gallardo, L. A., Markwitz, V., Ring, U., and S. N., Thomson. (2013), What caused
658 the denudation of the Menderes Massif: Review of crustal evolution, lithosphere structure,
659 and dynamic topography in southwest Turkey: Gondwana Research, 24(1), 243-274.

660 Gessner, K., Markwitz, V., and T., Güngör, (2017), Crustal fluid flow in hot continental
661 extension: tectonic framework of geothermal areas and mineral deposits in western
662 Anatolia. Geological Society, London, Special Publications, 453, SP453-7.
663 Gianelli, G. (2008). A comparative analysis of the geothermal fields of Larderello and Mt.
664 Amiata, Italy. Geothermal energy research trends. Nova Science, New York, 59-85.
665 Hetzel, R., Passchier, C. W., Ring, U. and O. O., Dora. (1995), Bivergent extension in orogenic
666 belts: the Menderes massif (southwestern Turkey): Geology, 23, 455-458.
667 Huet, B., Le Pourhiet, L., Labrousse, L., Burov, E., and L., Jolivet. (2011), Post-orogenic
668 extension and metamorphic core complexes in a heterogeneous crust: the role of crustal
669 layering inherited from collision. Application to the Cyclades (Aegean domain).
670 Geophysical Journal International, 184(2), 611-625.
671 Jolivet, L., Faccenna, C., Goffé, B., Mattei, M., Rossetti, F., Brunet, C., ... and T., Parra. (1998),
672 Midcrustal shear zones in postorogenic extension: example from the northern Tyrrhenian
673 Sea: Journal of Geophysical Research: Solid Earth, 103(B6), 12123-12160.
674 Jolivet, L., Famin, V., Mehl, C., Parra, T., Aubourg, C., Hébert, R., and P., Philippot. (2004),
675 Strain localization during crustal-scale boudinage to form extensional metamorphic domes
676 in the Aegean Sea: Geological Society of America Special Papers, 380, 185-210.
677 Jolivet, L., and J. P., Brun. (2010), Cenozoic geodynamic evolution of the Aegean. International
678 Journal of Earth Sciences, 99(1), 109-138.
679 Jolivet, L., Menant, A., Sternai, P., Rabillard, A., Arbaret, L., Augier, R., ... and L., Labrousse.
680 (2015), The geological signature of a slab tear below the Aegean: Tectonophysics, 659,
681 166-182.

682 Karabulut, H., Paul, A., Ergün, T. A., Hatzfeld, D., Childs, D. M., and M., Aktar. (2013), Long-
683 wavelength undulations of the seismic Moho beneath the strongly stretched Western
684 Anatolia: Geophysical Journal International, 194(1), 450-464.
685 Karamanderesi, İ. H., and C., Helvaci. (2003), Geology and hydrothermal alteration of the
686 Aydın-Salavatlı geothermal field, western Anatolia, Turkey. Turkish Journal of Earth
687 Sciences, 12(2), 175-198.
688 Kaya, A. (2015), The effects of extensional structures on the heat transport mechanism: An
689 example from the Ortakçı geothermal field (Büyük Menderes Graben, SW Turkey). Journal
690 of African Earth Sciences, 108, 74-88.
691 Koenig, J. B., and J.R., McNitt. (1983), Controls on the location and intensity of magmatic and
692 non-magmatic geothermal systems in the Basin and Range province: Geothermal
693 Resources Council (No. 13, p. 93). Special Report.
694 Labrousse, L., Huet, B., Le Pourhiet, L., Jolivet, L., and E., Burov. (2016), Rheological
695 implications of extensional detachments: Mediterranean and numerical insights: Earth-
696 Science Reviews, 161, 233-258.
697 Le Pourhiet, L., Burov, E., and I., Moretti. (2003), Initial crustal thickness geometry controls on
698 the extension in a back arc domain: Case of the Gulf of Corinth. Tectonics, 22(4).
699 Manning, C. E., & Ingebritsen, S. E. (1999). Permeability of the continental crust: Implications
700 of geothermal data and metamorphic systems. Reviews of Geophysics, 37(1), 127-150.
701 Menant, A., L. Jolivet, and B., Vrielynck. (2016a), Kinematic reconstructions and magmatic
702 evolution illuminating crustal and mantle dynamics of the eastern Mediterranean region
703 since the late Cretaceous: Tectonophysics, 675, 103-140;
704 doi:110.1016/j.tecto.2016.1003.1007.

Menant, A., Sternai, P., Jolivet, L., Guillou-Frottier, L., and T., Gerya. (2016b), 3D numerical modeling of mantle flow, crustal dynamics and magma genesis associated with slab roll-back and tearing: The eastern Mediterranean case. Earth and Planetary Science Letters, 442, 93-107.

Mezri, L., Le Pourhiet, L., Wolf, S., and E., Burov (2015), New parametric implementation of metamorphic reactions limited by water content, impact on exhumation along detachment faults, Lithos, 236-237, 287-298; http://dx.doi.org/210.1016/j.lithos.2015.1008.1021.

Moeck, I. S. (2014), Catalog of geothermal play types based on geologic controls. Renewable and Sustainable Energy Reviews, 37, 867-882.

Mulch, A., Teyssier, C., Cosca, M. A., and T. W., Vennemann. (2006), Thermomechanical analysis of strain localization in a ductile detachment zone: Journal of Geophysical Research: Solid Earth, 111(B12).

Oliver, N. H. S. (1996), Review and classification of structural controls on fluid flow during regional metamorphism: Journal of Metamorphic Geology, 14(4), 477-492.

Özen, T., Bülbül, A., and G., Tarcan. (2012), Reservoir and hydrogeochemical characterizations of geothermal fields in Salihli, Turkey. Journal of Asian Earth Sciences, 60, 1-17.

Ozdemir, A., Yasar, E., and G., Cevik. (2017), An importance of the geological investigations in Kavaklıdere geothermal field (Turkey). Geomechanics and Geophysics for Geo-Energy and Geo-Resources, 3(1), 29-49.

Piromallo, C., and A., Morelli. (2003), P wave tomography of the mantle under the Alpine-Mediterranean area. Journal of Geophysical Research: Solid Earth, 108(B2).

727 Rey, P.F., Teyssier, C., and D.L., Whitney. (2009), The Role of Partial Melting and Extensional
728 Strain Rates in the Development of Metamorphic Core Complexes, in Chardon, D., Rey,
729 P., Teyssier, C., and Whitney, D.L., eds., Hot Orogen: Tectonophysics, v. 477, p. 135–144.
730 Reynolds, S. J., and G. S., Lister. (1987), Structural aspects of fluid-rock interactions in
731 detachment zones: Geology, 15(4), 362-366.
732 Roche, V., Bouchot, V., Beccaletto, L., Jolivet, L., Guillou-Frottier, L., Tuduri, J., Bozkurt, E.,
733 Oguz, K., and B., Tokay. (submitted), Structural, lithological and geodynamic controls on
734 geothermal activity in the Menderes geothermal Province (Western Anatolia, Turkey):
735 IJES.
736 Ricard, Y., and C., Froidevaux. (1986), Stretching instabilities and lithospheric boudinage:
737 Journal of Geophysical Research: Solid Earth, 91(B8), 8314-8324.
738 Santilano, A., Manzella, A., Gianelli, G., Donato, A., Gola, G., Nardini, I., ... and S., Botteghi.
739 (2015), Convective, intrusive geothermal plays: what about tectonics?. Geothermal Energy
740 Science, 3(1), 51-59.
741 Schellart, W. P., Stegman, D. R., Farrington, R. J., Freeman, J., and L., Moresi. (2010),
742 Cenozoic tectonics of western North America controlled by evolving width of Farallon
743 slab. Science, 329(5989), 316-319.
744 Schubert, G., and Yuen, D. A. (1978), Shear heating instability in the Earth's upper mantle.
745 Tectonophysics, 50(2-3), 197-205.
746 Sibson, R. H., Moore, J. M. M., and A. H., Rankin. (1975), Seismic pumping—a hydrothermal
747 fluid transport mechanism: Journal of the Geological Society, 131(6), 653-659.

748 Sternai, P., L. Jolivet, A. Menant, and T., Gerya. (2014), Driving the upper plate surface
749 deformation by slab rollback and mantle flow: Earth Planet. Sci. Lett., 405, 110–118,
750 doi:10.1016/j.epsl.2014.08.023.
751 Tirel, C., Gueydan, F., Tiberi, C., and J.P., Brun. (2004), Aegean crustal thickness inferred from
752 gravity inversion. Geodynamical implications. Earth and Planetary Science Letters, 228(3),
753 267-280.
754 Wannamaker, P. E., Hasterok, D. P., Johnston, J. M., Stodt, J. A., Hall, D. B., Sodergren, T. L.,
755 ... and M. J., Unsworth. (2008), Lithospheric dismemberment and magmatic processes of
756 the Great Basin–Colorado Plateau transition, Utah, implied from magnetotellurics.
757 Geochemistry, Geophysics, Geosystems, 9(5).
758

759 **APPENDIX**

760 1. Supplementary Figures and Videos

761

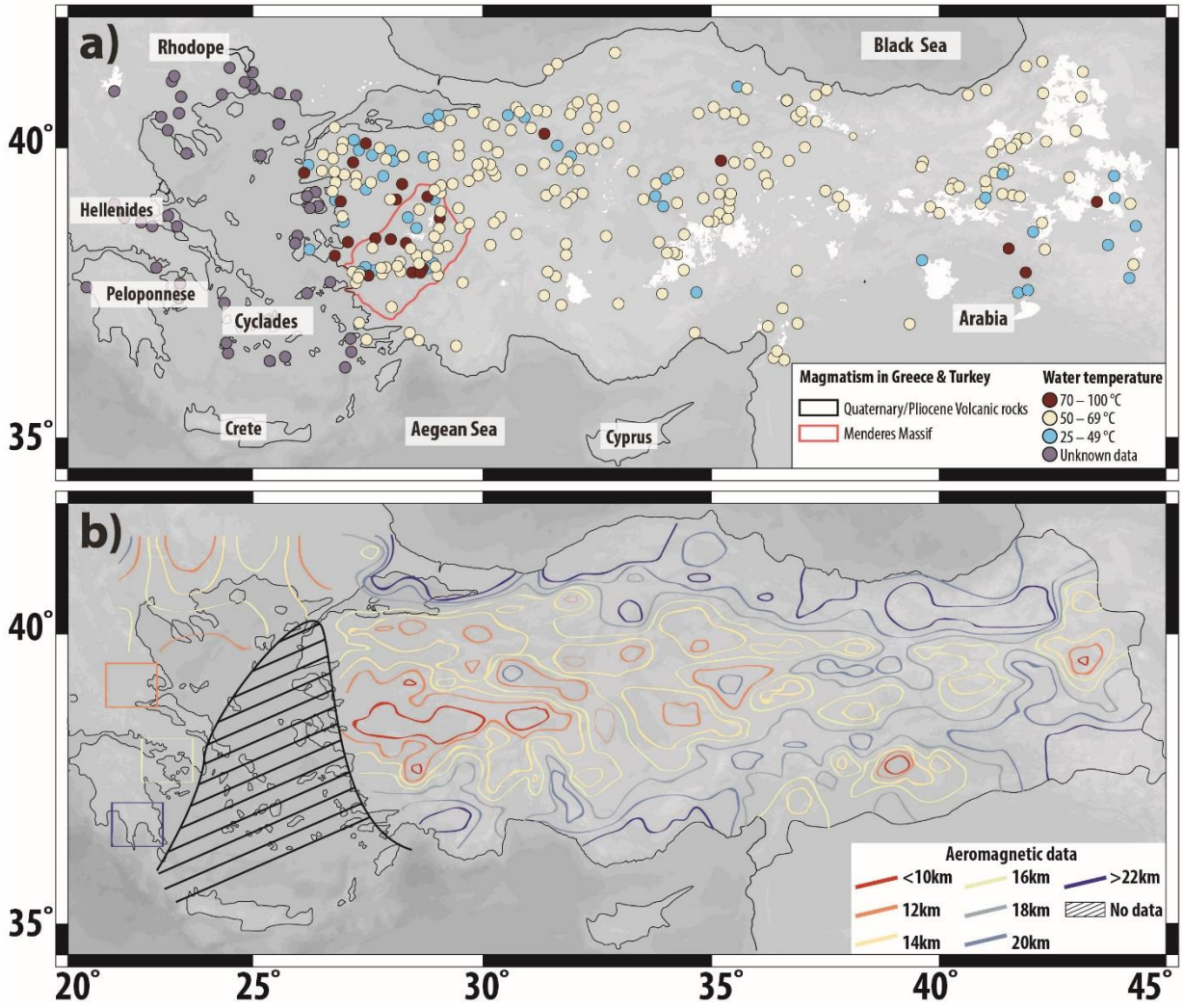

762

763 Figure S1: Maps of the Aegean-Anatolian region. (a) Geothermal map of eastern Mediterranean
764 region highlighting major thermal occurrences based on a compilation of several data sources
765 (from the MTA (2005); Mendrinos *et al.* (2010) and Andritsos *et al.* (2015)), and spatial
766 distribution of Pliocene-Quaternary volcanic rocks (from the geological map of the MTA). (b)

767 Curie-point depth map from Tselentis (1991); Stampolidis and Tsokas (2002) and Aydin *et al.*

768 (2005).

769

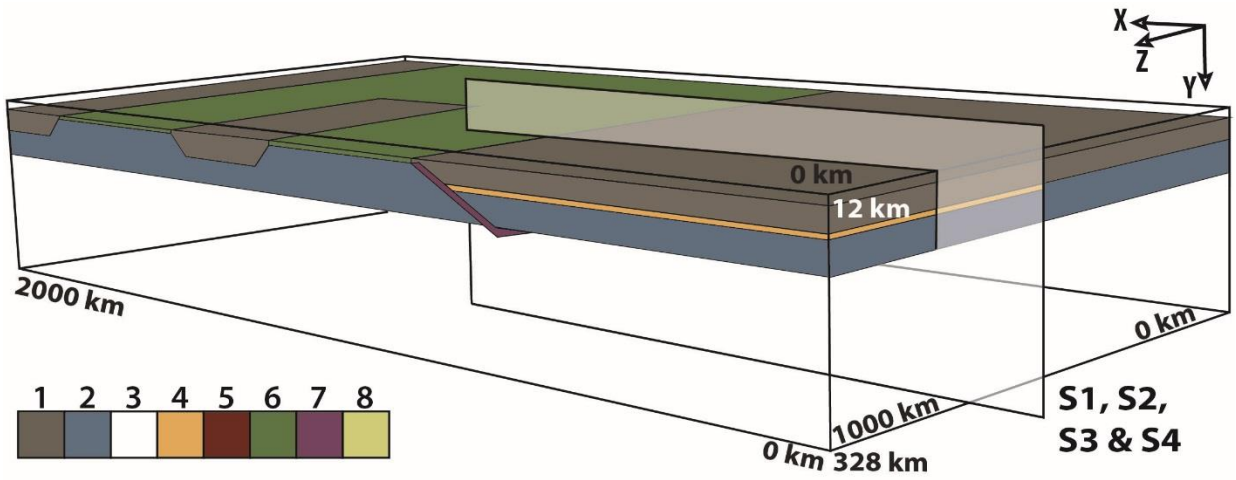

770

771 Figure S2: Location of videos shown by the vertical cross-section from our reference numerical

772 model. Colours showing different rock types: 1-2-3-4-5-6-7-8 as defined in Figure 3.

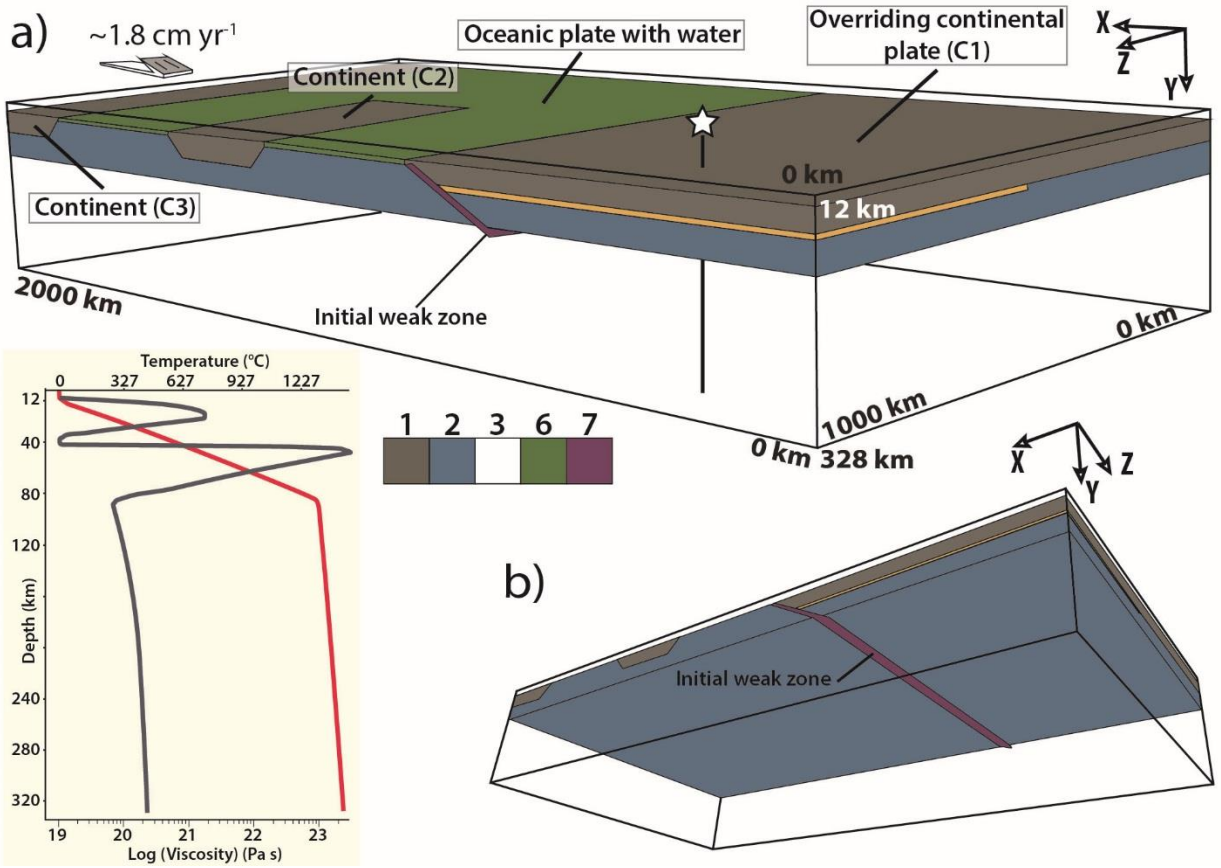

Figure S3: Experimental setup without slab tearing. (a) 3D initial model setup where the top layer ("sticky air", y < ~ 12 km") and the water are cut off for clarity. Colours showing different rock types as defined in Figure 3. Vertical viscosity (grey) and temperature (red) profiles at t_0, taken at the location shown by the white star. (b) Location of the "weak zone" (i.e. hydrated/serpentinized mantle) into the lithosphere to initialise subduction (z-parallel).

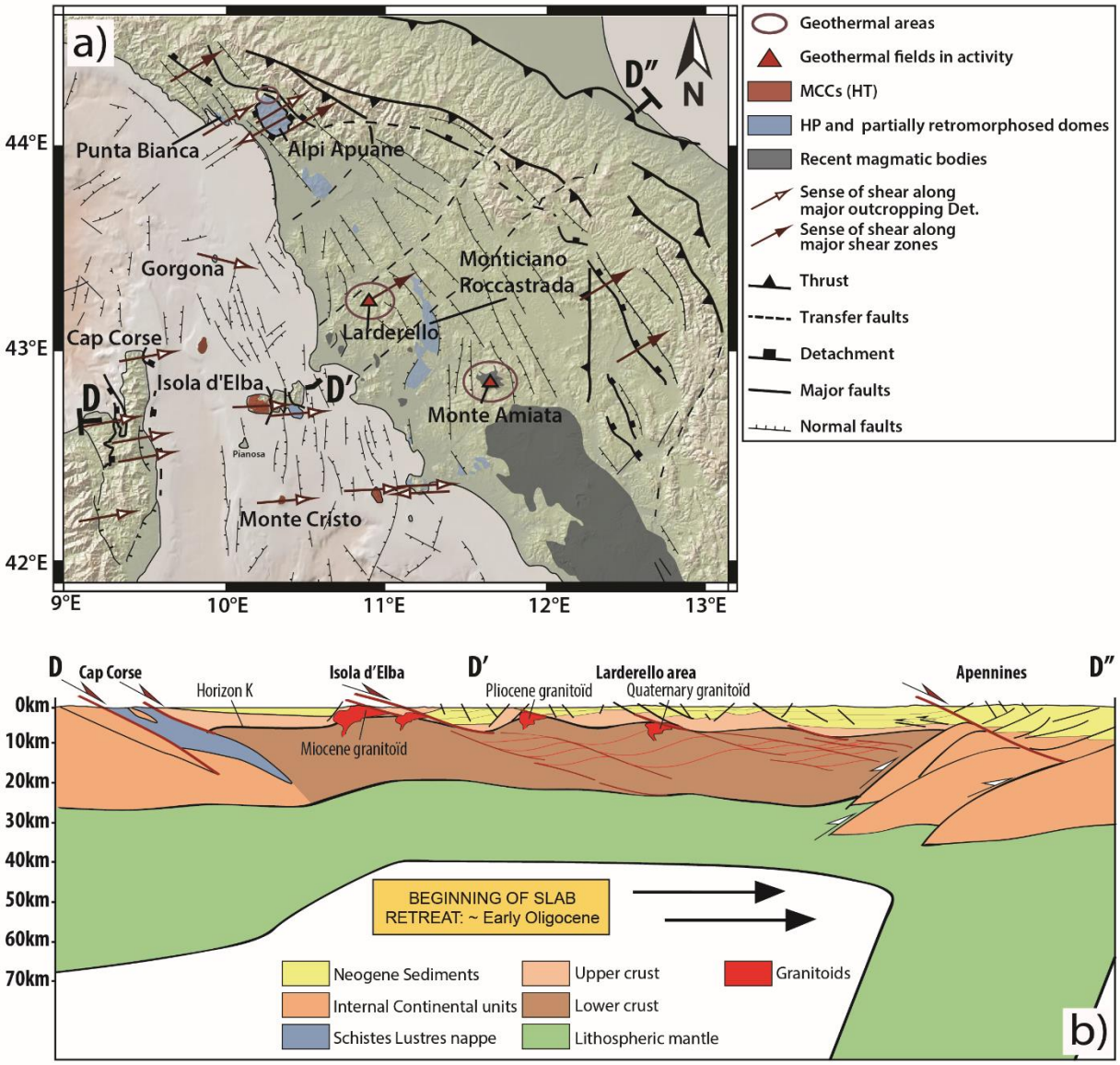

Figure S4: Simplified tectonic map showing the main metamorphic core complexes and associated detachments faults. (a) Map of the Northern Tyrrhenian region and Northern Apennines, modified from Jolivet *et al.* (1998). (b) Simplified cross-sections highlighting slab retreat and formation of crustal detachments.

Videos S1 – S4 showing the ascent of partially molten material (the yellowish color), the thermal domes, the composition and the second invariant of the strain rate tensor evolution, respectively.

Note that the location of the modeled arc in our numerical model is the position of mantle upwellings (i.e. molten material) projected at the surface. Even if the distance between arc and trench changes in time and space, note that the distance should be around 100 – 150 km from the trench toward the upper plate.

2. Supplementary materials

2.1. 3-D numerical approach

Continuity and momentum equations

The code I3ELVIS uses a staggered finite difference scheme combined with the marker-in-cell technique (Gerya, 2010). Lagrangian advecting markers are thus combined with an immobile Eulerian grid. The incompressible continuity equation describes the conservation of mass during the deformation of a continuous medium (rocks) as:

$$div(\vec{v}) = 0, \quad (2)$$

where $\vec{v}$ is the local velocity and div() is the divergence operator.

The conservation of momentum is obtained through the solution of the Stokes equation:

$$\frac{\partial \sigma'_{ij}}{\partial x_j} - \frac{\partial P}{\partial x_i} + \rho g_i = 0, \quad (3)$$

where i and j denote the coordinate indices (i.e. x, y, z), σ' is the deviatoric stress tensor, x_i and x_j are the spatial coordinates and g_i is the i^{th} component of the gravity vector $\vec{g}$.

Heat conservation equation

In order to predict changes in temperature due to heat transport, the Lagrangian heat conservation equation is solved, which consider conductive heat transport, as well as internal heat generation:

$$\rho C_p \frac{DT}{Dt} = -\frac{\partial q_i}{\partial xi} + H,$$

(4)

where the heat flux vector $\vec{q}$ is related to the temperature gradient in space as:

$$q_i = -k \frac{\partial T}{\partial x_i}.$$

(5)

T is temperature and *k* is the thermal conductivity of the material, which depends on pressure (*P*), *T*, and composition of the material. *Cp* is the isobaric heat capacity, $\frac{DT}{Dt}$ is the substantive time derivative of temperature and *H* is the volumetric heat productions. The latter term includes several types of heat generation/consumption processes:

$$H = H_r + H_s + H_a ,$$

(6)

where H_r is the radiogenic heat production, H_s is the shear heating and H_a is the adiabatic heat production. H_s is related to dissipation of the mechanical energy during irreversible non-elastic (e.g. viscous) deformation. It is calculated as:

$$H_s = \sigma'_{ij} \dot{\varepsilon}'_{ij} ,$$

(7)

where $\dot{\varepsilon}'$ is the strain rate tensors. H_a corresponds to heat production related to pressure changes. It is calculated as:

$$H_a = T\alpha \frac{DP}{Dt}, \quad (8)$$

where $\frac{DP}{Dt}$ is the substantive time derivative of pressure. Advection of temperature is performed by using Lagrangian markers (Gerya, 2010).

Viscous rheology of rocks

The physical properties of rocks used in our experiments are given in Table 1. Among them, the density of solid rocks depends on *P*, *T*, and composition. In our experiments, ρ_{solid} is calculated as follow:

$$\rho_{solid} = \rho_{0solid}\,[1 + \beta(P - P_r)] * [1 - \alpha(T - T_r)], \quad (9)$$

where ρ_{0solid} is the standard density of solid rocks at reference pressure P_r (10^5 Pa = 1 bar) and temperature T_r (298.15 K = 25 °C); α and β are respectively the thermal expansion and compressibility of rock. As density is also modified by phase changes (such as partial melting which is implemented in this code), effective rock density ρ_{eff} is calculated as follow:

$$\rho_{eff} = \rho_{solid}\,(1 - M + M\frac{\rho_{0molten}}{\rho_{0solid}}), \quad (10)$$

where $\rho_{0molten}$ is the standard density of molten rock, and *M* is the volumetric melt fraction in partially molten rock (see below for more information). In addition, non-Newtonian visco-plastic rheologies used in our experiments are implemented by both ductile and brittle/plastic

experimentally constrained laws. Effective viscosity for dislocation creep thus depends on the strain rate, pressure and temperature. It is calculated as follow:

$$\eta_{creep} = \dot{\varepsilon}_{II}^{\frac{1-n}{n}} A_D^{\frac{-1}{n}} \exp\left(\frac{E+P\,V}{n\,R\,T}\right), \quad (11)$$

where $\dot{\varepsilon}_{II}$ is the square root of the second invariant of the strain rate tensor, R is the gas constant, n is the creep exponent, A_D is the pre-exponential factor, E is the activation energy) and V is the activation volume. These parameters depend on the applied viscous flow law (i.e. wet quartzite, plagioclase (An_{75}), dry olivine and wet olivine flow laws; Table 1) (*Ranalli*, 1995). This ductile behavior is limited with a brittle/plastic one, implemented by using the Drucker-Prager criterion σ_{yield} (i.e. plastic strength) (*Ranalli*, 1995) as follow:

$$\eta_{creep} \leq \frac{\sigma_{yield}}{2\dot{\varepsilon}_{II}}, \quad (12)$$

where σ_{yield} is calculated as:

$$\sigma_{yield} = \sigma_C + P\sin(\varphi), \quad (13)$$

where σ_C is the compressive strength of the rock, P is the dynamic pressure and φ is the effective internal friction angle depending on the fluid and melt presence (see details in Gerya and Meilick (2011)).

Fluid/melt dynamics: example of partial melting

In our experiments, partial melting process is also included. For all crustal rocks, the volumetric melt fraction (M_0) is calculated as follow:

$M_0 = 0$ at $T < T_{solidus}$

$$M_0 = \frac{T - T_{solidus}}{T_{liquidus} - T_{solidus}} \text{ at } T_{solidus} < T < T_{liquidus} \quad (14)$$

$$M_0 = 1 \text{ at } T > T_{liquidus}$$

where M_0 is the volumetric fraction of melt with no previous melt extraction, $T_{solidus}$ and $T_{liquidus}$ are, respectively, the solidus and liquidus temperatures depending on the pressure and rock composition (Table 1). For the mantle, the degree of partial melting depends on the water content according to the parameterization of Katz *et al.* (2003). Resulting partially molten rocks can then undergo a succession of melt extraction episodes depending on their melt extraction threshold M_{max} and non-extractable melt fraction M_{min}, both equal to 1%. Only the exceeding volumetric melt fraction (i.e. > 1 %) is then extracted from partially molten rocks, thus generating magma markers. For each extraction episode, the melt fraction M_{ext} recorded in the partially molten rock markers is calculated as:

$$M_{ext} = M - M_{min}, \quad (15)$$

where M is the volumetric melt fraction in partially molten rock, accounting for previous melt extraction events. It is calculated as:

$$M = M_0 - \Sigma M_{ext}, \quad (16)$$

where ΣM_{ext} is the total melt fraction from previous extraction episodes. Then, M varies dynamically until remaining solid rock is no longer able to undergo additional partial melting (i.e. $\Sigma M_{ext} > M_0$). Magma markers resulting from these extraction episodes are then instantaneously transmitted to the surface as free melt is assumed to propagate upward much faster than rocks deform (Hawkesworth, 1997).

Material	k	Hr	ρ_0	C_P	E_a	V_a	α	β	n	η_0	Viscous flow law	sin (Φ_{eff})
	(W m^{-1} K^{-1})	(mW m^{-3})	(kg m^{-3})	(J kg^{-1} K^{-1})	(kg mol^{-1})	(m^3 mol^{-1})	(K^{-1})	(kbar^{-1})		(Pa^n s)		
Sticky-air	20	0	1	100	0	0	0	0	1	$1x10^{19}$	Air	0
Water	20	0	1000	3330	0	0	0	0	1	$1x10^{19}$	Water	0
Sediment	0.64+807/(T+77)	2	2600	1000	154	8	$3x10^{-5}$	$1x10^{-3}$	2.3	$1.97x10^{17}$	Wet Qz.	0.15
Cont. Crsut (C1 & C3)	0.64+807/(T+77)	2	2750	1000	154	8	$3x10^{-5}$	$1x10^{-3}$	2.3	$1.17x10^{17}$	Wet Qz.	0.15
Cont. Crsut (2)	1.18+807/(T+77)	2	2950	1000	238	8	$3x10^{-5}$	$1x10^{-3}$	3.2	$4.8x10^{22}$	Wet Qz.	0.15
Oc. Crust	1.18+474/(T+77)	0.25	3000	1000	238	8	$3x10^{-5}$	$1x10^{-3}$	3.2	$4.8x10^{22}$	Wet Qz.	0.15
Mantle	0.73+1293/(T+77)	0.02	3300	1000	532	8	$3x10^{-5}$	$1x10^{-3}$	3.5	$3.98x10^{16}$	Dry Ol.	0.6
Weak zone	0.73+1293/(T+77)	0.05	3300	1000	47	8	$3x10^{-5}$	$1x10^{-3}$	4	$5x10^{20}$	Wet Ol.	0

Table 1: Material properties used in the numerical experiments. k denotes the thermal conductivity, H_r is the radiogenic heat production, ρ_0 is the density, C_p is the specific heat capacity, E_a is the activation energy, V_a is the activation volume, α is the thermal expansion, β is the compressibility coefficient, n is the stress exponent, η_0 is the reference viscosity and Φ_{eff} is the effective internal friction angle. Qz. and Ol. correspond to the abbreviations of Quartzite and Olivine.

2.2. 2-D numerical approach

The numerical model presented in Figures 7 and 8 has been built on the same basis as those published by Guillou-Frottier *et al.* (2013). Darcy's law is coupled with the heat equation in a porous medium and with mass conservation. We have used the Comsol Multiphysics™ software, where temperature-dependent properties can be easily implemented. Benchmark experiments have already been performed and published (Garibaldi *et al.*, 2010).

The numerical mesh consisted in more than 32,000 triangles, with a maximum size of 40 m within the detachment. Petrophysical properties are given in Table 2. Fluid density law was chosen to fit the experimental data for pure water between 20 and 350 °C:

$$\rho_L(T) = 1002.4 - 0.1905 * T - 0.0025 * T^2 \quad (17)$$

where T is temperature in °C and ρ_L the fluid density in kg m^{-3}. For temperature greater than 350°C, fluid density is assigned a constant value of 630 kg m^{-3}. This choice has no fundamental consequences on the results since at these high temperatures, fluid is located at depth greater than 5 km, where permeability does not allow fluid circulation. For the fluid dynamic viscosity, the law used has been written as:

$$\mu(T) = 2.414\ 10^{-5} \times \exp\left(\frac{570}{T+133}\right) \quad (18)$$

where T is in °C and dynamic viscosity μ is in Pa s.

The initial pressure field increases linearly with depth. The initial temperature field is computed in a conductive regime, such that the surface temperature is 20 °C and the bottom of the box (10 km depth) is close to 500 °C, as it is suggested by Aydin *et al.* (2005). To reach a temperature around ~ 500 °C at a depth of 10 km, a basal heat flow of 120 mW m^{-2} is imposed during the transient behaviour. At t > 0, permeability values (see Table 2) are affected to the two units, and transient evolution of temperature and velocity fields are recorded. The chosen permeability law accounts for depth-dependence reaching a low value (~ 10^{-18} m^2) at the brittle-ductile transition, as suggested by Violay *et al*. (2017).

	Basement	**Detachment**
Eq. thermal conductivity(*)	2.8	1.6
Porosity (%)	5	30
Permeability (**) (m^2)	$[10^{-17} – 10^{-14}]\exp((z-2000)/1000)$	$[10^{-17} – 10^{-14}]$

Heat production ($\mu W.m^{-3}$)	1.0	0

Table 2: Material properties used in the numerical experiments. (*) the equivalent thermal conductivity accounts for solid matrix and fluid-filled pores. (**) permeability decreases exponentially with depth, except in the detachment.

REFERENCES

Andritsos, N., Dalambakis, P., Arvanitis, A., Papachristou, M., & Fytikas, M. (2015). Geothermal developments in Greece–Country update 2010-2014. In Proceedings World Geothermal Congress 2015 (pp. 19-24).

Aydın, İ., Karat, H. İ., & Koçak, A. (2005). Curie-point depth map of Turkey. Geophysical Journal International, 162(2), 633-640.

Garibaldi, C., Guillou-Frottier, L., Lardeaux, J.M., Bonté, D., Lopez, S., Bouchot, V., & P., Ledru. (2010). Thermal anomalies and geological structures in the Provence basin : implications for hydrothermal circulations at depth. Bulletin de la Société Géologique de France 181, 363-376.

Gerya, T. V., & F. I. Meilick (2011). Geodynamic regimes of subduction under an active margin: effects of rheological weakening by fluids and melts, J. Metamorph. Geol., 29(1), 7–31, doi:10.1111/j.1525-1314.2010.00904.x.

Guillou-Frottier, L., Carrė, C., Bourgine, B., Bouchot, V., & A., Genter. (2013). Structure of hydrothermal convection in the Upper Rhine Graben as inferred from corrected

953 temperature data and basin-scale numerical models. Journal of Volcanology and
954 Geothermal Research, 256, 29-49.
955 Hawkesworth, C. J. (1997). U-Th Isotopes in Arc Magmas: Implications for Element Transfer
956 from the Subducted Crust, Science, 276(5312), 551–555,
957 doi:10.1126/science.276.5312.551.
958 Katz, R. F., Spiegelman, M., & Langmuir, C. H. (2003). A new parameterization of hydrous
959 mantle melting. Geochemistry, Geophysics, Geosystems, 4(9).
960 Mendrinos, D., Choropanitis, I., Polyzou, O., & Karytsas, C. (2010). Exploring for geothermal
961 resources in Greece. Geothermics, 39(1), 124-137.
962 MTA, Geothermal Energy Projects Reports (1970-2008).
963 Ranalli, G. (1995). Rheology of the Earth, Chapman & Hall., London, UK.
964 Stampolidis, A., & Tsokas, G. N. (2002). Curie point depths of Macedonia and Thrace, N.
965 Greece. Pure and Applied Geophysics, 159(11), 2659-2671.
966 Tselentis, G. A. (1991). An attempt to define Curie point depths in Greece from aeromagnetic
967 and heat flow data. pure and applied geophysics, 136(1), 87-101.
968 Violay, M., Heap, M. J., Acosta, M., & Madonna, C. (2017). Porosity evolution at the brittle-
969 ductile transition in the continental crust: Implications for deep hydro-geothermal
970 circulation. Scientific reports, 7(1), 7705.
971
972